JOURNAL OF GEOPHYSICAL RESEARCH, VOL. 99, NO. E7, PAGES 14,623-14,658, JULY 20, 1994

# Belt-zone variations in the Jovian cloud structure

Barbara E. Carlson, Andrew A. Lacis, and William B. Rossow
Goddard Institute for Space Studies, New York

**Abstract.** Voyager IRIS observations of Jupiter in the far infrared (180–1200 $cm^{-1}$) are sensitive to emission originating from pressures less than 2 bars, while the 5-$\mu$m (1800–2300 $cm^{-1}$) observations are primarily sensitive to emission originating from pressures greater than 2 bars. We use these differences in the location of the peak emission level to constrain the properties of the upper tropospheric cloud structure from the far-infrared observations and then use the 5-$\mu$m observations, with the upper tropospheric cloud structure fixed, to constrain the deep cloud structure. The relationship between observed 45- and 5-$\mu$m brightness temperatures reveals three distinct regions between ±25° latitude: North Equatorial Belt hot spots, which are "hot" at both 45 and 5 $\mu$m; Equatorial Zone spectra, which are "warm" at 45 $\mu$m and "cold" at 5 $\mu$m; and North Tropical Zone spectra, which are "cold" at both 45 and 5 $\mu$m. We find that the hot extreme spectral ensemble is unique to belts, and the cold extreme spectral ensembles are unique to zones, but that all other intermediate spectral ensembles are common to both regions. Analyses of these spectra using an anisotropic multiple scattering radiative transfer model reveal that the primary difference between belts and zones is the increased opacity and vertical extent of clouds in zones relative to their belt counterparts. In addition, we find a shift in the location of the para hydrogen gradient toward lower pressures in zones, with an increase in the "equilibrated" cloud-top para fraction. We suggest that all of the variations in gas abundance profiles, temperature, and cloud structure are consistent with the effects of a simple mean circulation and large-scale wave motions.

## 1. Introduction

Photographic images of Jupiter show a complicated and spatially inhomogeneous atmosphere [*Gehrels*, 1976; *Smith et al.*, 1979]. Clouds and some additional chromophore(s) play a key role in defining our image of Jupiter. Belts and zones are primarily distinguished on the basis of shading, with belts corresponding to "dark" regions and zones corresponding to "light" regions. Yet the actual visual contrast is much smaller than that suggested by the contrast-stretched Voyager images; it is only of the order of 10%.

In the mean circulation, belts and zones are observed to correspond to anticyclonic and cyclonic motions, respectively. To reconcile this with "lighter" and "darker" condensate clouds that are determined by vertical motions, these clouds are thought to be in the upper part of upwelling (zones) and downwelling (belts) regions [*Hess and Panofsky*, 1951; *Stone*, 1976; *Williams*, 1985]. One factor complicating this understanding of the Jovian belt-zone structure is that the appearance of the planet has been observed to change dramatically with time. Comparison between the Pioneer [*Fountain et al.*, 1974] and Voyager [*Smith et al.*, 1979] images shows major changes in the appearance of the South Tropical Zone. In the 1974 Pioneer images, this region is a broad, featureless "white" zone in contrast with its banded, more beltlike appearance in the 1979 Voyager images. A comparable, though opposite, change occurred in the North Tropical Zone, which in the Pioneer images was considerably less uniform than in the Voyager images. Temporal variations have also been observed in belts. A recent example was the apparent "clouding over" (brightening) of the South Equatorial Belt in July 1989. As late as April 1989, this belt was a prominent feature [*Lutz and Gullixson*, 1989]. No large associated changes in the mean zonal wind speed have been found, though the time coverage is very poor.

These temporal variations, combined with the small contrast in reflectivity at visible wavelengths between belts and zones, suggest that the differences, at least in terms of cloud structure, are actually small. Additional support for this notion comes from the similarity of the Voyager infrared interferometer spectrometer (IRIS) observations of the warmer regions within zones and the colder regions within belts, as discussed in section 2. Nevertheless, the colder regions within zones are characteristically different from the warmer regions within belts. We use these characteristic differences to explore the nature of the belt-zone differences in terms of the atmospheric structure and its implications for the mean circulation.

In section 2 we use spatial variations of the correlation between observed 45- and 5-$\mu$m brightness temperatures to refine the concept of belt versus zone and to select homogeneous spectral ensembles for detailed radiative transfer analysis. For our analysis, we use an anisotropic multiple scattering radiative transfer model [*Carlson et al.*, 1993], which is described in section 3 along with a discussion of the spectral sensitivity to the retrieved parameters. We present the results of this investigation in section 4 and discuss some implications of these inferred belt-zone differences in section 5.



Paper number 94JE01222.

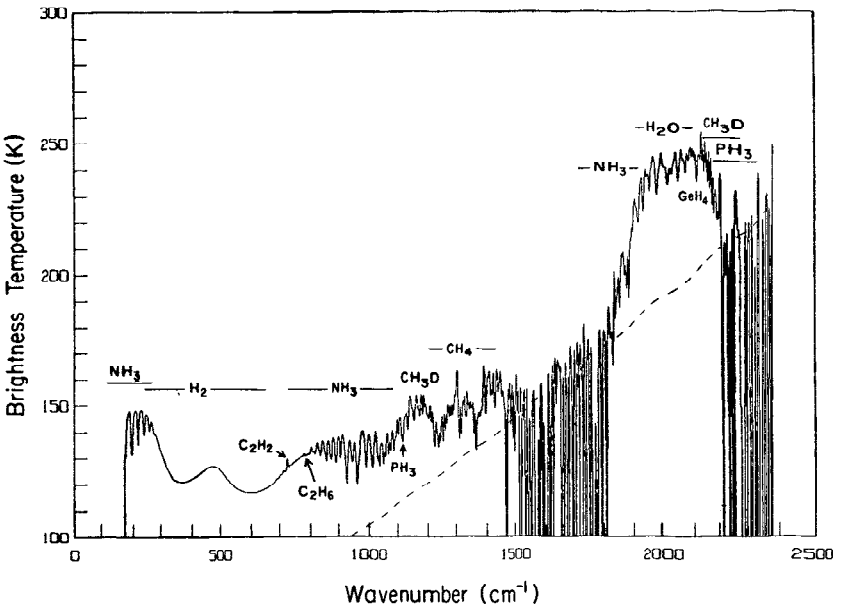


**Figure 1.** Average NEB IRIS spectrum. The average noise equivalent brightness temperature is shown as a dashed line. Gaseous absorptions are indicated.

## 2. Observations

The Voyager 1 IRIS instrument obtained measurements over the 180–2500 $cm^{-1}$ (4–55 $\mu$m) spectral interval with an apodized spectral resolution of 4.3 $cm^{-1}$. The average noise equivalent radiance of an individual spectrum falls steeply from $3 \times 10^{-8}$ W $cm^{-2}$ $sr^{-1}/cm^{-1}$ at 180 $cm^{-1}$ to a minimum of $4 \times 10^{-9}$ at 400 $cm^{-1}$; thereafter it rises nearly linearly to $1.2 \times 10^{-8}$ W $cm^{-2}$ $sr^{-1}/cm^{-1}$ at 2000 $cm^{-1}$ [*Hanel et al.*, 1979]. One of the key advantages of the IRIS data set is the high wavelength-to-wavelength precision of the measurements. A sample IRIS spectrum (solid line) is shown in Figure 1 along with the noise equivalent brightness temperature (dashed line) of the IRIS measurements.

The noise equivalent brightness temperature of the IRIS observations, the dashed line in Figure 1, divides the IRIS spectrum into two sections, since the generally low signal-to-noise ratio of the measurements in the 1500–1800 $cm^{-1}$ region precludes their use. Radiation in the far-infrared (180–1200 $cm^{-1}$) region of the spectrum originates at pressures less than 1.5 bars, while radiation in the 5-$\mu$m (1800–2300 $cm^{-1}$) region of the spectrum originates at greater depth and higher temperatures.

The locations of the gaseous absorption features are also indicated in Figure 1. The far-infrared region is dominated by the S(0) and S(1) hydrogen lines located at 350 and 602 $cm^{-1}$, respectively. Emission features produced by acetylene at 729 $cm^{-1}$ and ethane at 826 $cm^{-1}$ are apparent in the IRIS observations. These features are stratospheric in origin and are not included in this investigation.

Based on the results of thermochemical equilibrium models [e.g., *Weidenschilling and Lewis*, 1973; *Carlson et al.*, 1987], three clouds are predicted to form in the Jovian atmosphere. Previous investigations [e.g., *Bézard et al.*, 1983] have noted that a correlation exists between observed 45- and 5-$\mu$m brightness temperatures. This correlation suggests that a vertical association exists between variations in the deep cloud structure ($NH_4SH$ and $H_2O$ clouds) and the upper tropospheric $NH_3$ cloud layer. In this section, we explore the nature of the observed correlation.

The Voyager incoming and outgoing mapping sequences provide nearly uniform spatial coverage of Jupiter [*Hanel et al.*, 1979]; however, the circular field of view (FOV) of these observations is ≈10° latitude, which is not sufficient to resolve the individual belts and zones comprising the planetary-scale features. Nevertheless, we can use the mapping sequence observations to provide a framework within which we can interpret the higher spatial resolution observations obtained during the "encounter" period. Figure 2 compares the spatial distribution of the mapping sequence observations (Figure 2a) to the higher spatial resolution encounter observations (Figure 2b). The characters plotted mark the locations of the centers of the IRIS fields of view. Since we restrict the emission angle to be less than 30°, corresponding to $\mu$ (cosine of the emission angle) greater than 0.866, the observations correspond to near-nadir viewing. To ensure homogeneity, this emission angle selection criterion forces us to impose an additional latitudinal selection criterion on the mapping sequence observations, limiting our investigation to the region between ±25° latitude. From the comparison in Figure 2, we see that this region is well sampled in both subsets of the IRIS observations. This latitude range contains the North Tropical Zone (NTrZ), the North Equatorial Belt (NEB), the Equatorial Zone (EqZ), the South Equatorial Belt (SEB), and the South Tropical Zone (STrZ). The latitudinal boundaries that we have used to define these regions are given in Table 1.

To investigate the effects of spatial averaging over the IRIS field of view and small-scale (subpixel) inhomogeneities on the observed brightness temperatures, we make use of the field of view variability inherent in the mapping sequence and encounter observations. Figure 3 shows a comparison between the observed 45 $\mu$m (Figure 3a) and 5 $\mu$m (Figure 3b) brightness temperature distributions for the lower spatial resolution mapping sequence (top panels) and the higher

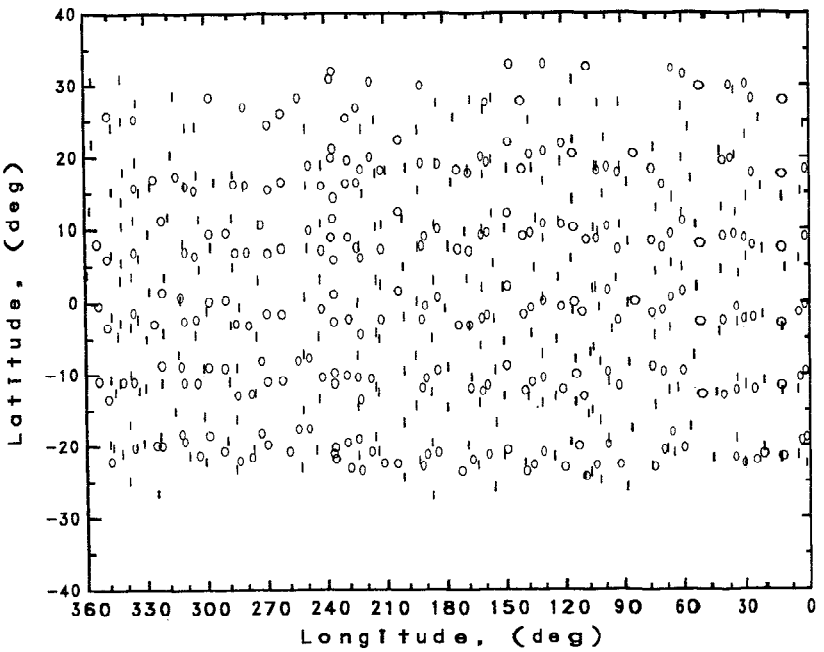


**Figure 2a.** Spatial distributions of the incoming (I) and outgoing (O) mapping sequence observations. The emission angle is restricted to less than 30° here and in Figure 2b.

spatial resolution encounter observations (lower panels). The 45-$\mu$m spectral region, defined here to be 226 ± 4 $cm^{-1}$, is expected to be a good indicator of variations in $NH_3$ cloud opacity, while the 5-$\mu$m region, defined here to be the average over the interval 1950 ± 100 $cm^{-1}$, is expected to be a good indicator of variations of the $NH_4SH$ and $H_2O$ cloud opacity. As might be expected in a horizontally inhomogeneous atmosphere, the higher spatial resolution encounter observations exhibit more structure in their distribution of values as well as more extreme brightness temperatures. Thus the larger FOV of the mapping sequence observations has the effect of spatially averaging over the brightness temperature extremes seen at higher spatial resolution. At the higher spatial resolution of the encounter observations, there is an indication of warm and cold subgroups in both the 45-$\mu$m and 5-$\mu$m brightness temperature histograms.

To investigate whether or not these warm and cold subgroups are associated with the planetary-scale belt-zone system, the encounter observations can be sorted into latitudinal categories to isolate the individual belts and zones. In

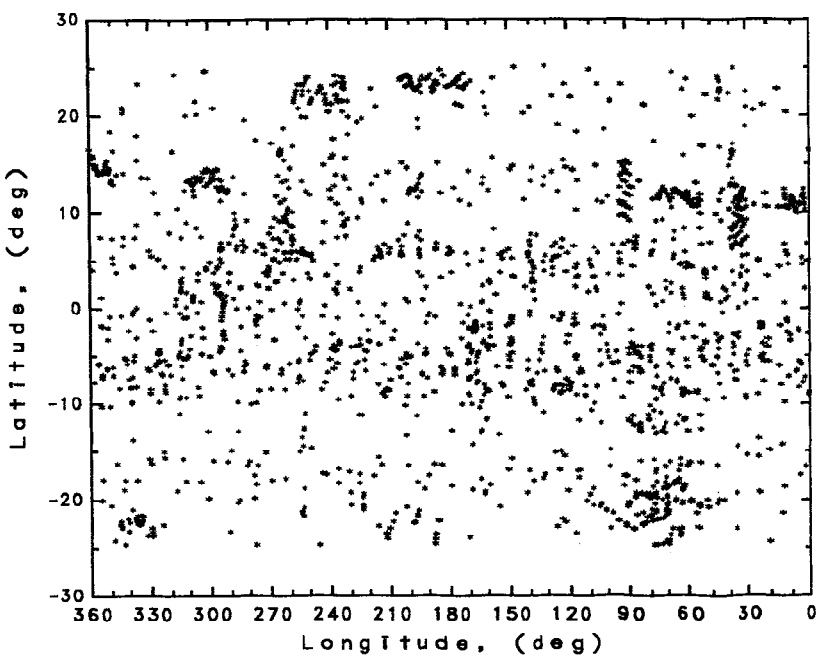


**Figure 2b.** Higher spatial resolution encounter observations.

**Table 1.** Latitudinal Extent of the Belts and Zones

| Region | Latitude Range, deg |
|---|---|
| NTrZ | 17–23 |
| NEB | 7–13 |
| EqZ | −3–3 |
| SEB | −7 to −13 |
| STrZ | −17 to −23 |

Figure 4 we compare the brightness temperature histograms at 45- and 5-$\mu$m for two FOV size ranges. All of these observations have an FOV less than 5° latitude sufficient to resolve the planetary-scale belt-zone structure, but the inclusion of the shaded distribution, FOVs less than 3° latitude, allows us to further investigate the dependence of our results on spatial resolution. Due to the geometry of the observations, there are no observations of the STrZ with a FOV of less than 3° latitude. (Since we are interested in the belt-zone structure, we have excluded observations that include the Great Red Spot within the IRIS FOV.)

The 45-$\mu$m measurements (Figure 4a) reveal that the NEB and SEB distributions are hotter than those for the NTrZ, EqZ, and STrZ. Of the zones, the NTrZ has the coldest 45-$\mu$m brightness temperature distribution. The distribution of brightness temperatures observed in the NTrZ does not overlap that found in belts; however, the range of brightness temperatures found in the EqZ and STrZ does overlap the brightness temperature distribution found in belts. With increasing spatial resolution the mean temperature of the belt distribution increases while the mean temperature of the zone distribution decreases. Even at the higher spatial resolution, the range of brightness temperatures found in zones still overlaps that found in belts. The STrZ brightness temperature distribution has two components; one that is EqZ-like and the other than is NTrZ-like. The 45-$\mu$m brightness temperatures suggest that two distinct subgroups exist which can be represented by the NTrZ and the NEB/SEB.

The 5-$\mu$m measurements (Figure 4b) reveal a similar pattern, with the NEB and SEB distributions hotter than those in the NTrZ, EqZ, and STrZ. Of the zones, the NTrZ again has the coldest distribution. Moreover, with increasing spatial resolution the mean temperatures of the belt distributions increase while the mean temperatures of the zone distributions decrease. Comparing all five brightness temperature distributions, there are some indications of a split in the 5-$\mu$m brightness temperature behavior with a zonelike distribution at brightness temperatures less than 210 K (i.e., NTrZ-like) and a beltlike distribution at brightness temperatures larger than 220 K (i.e., SEB-like). As was found for the 45-$\mu$m brightness temperatures, the 5-$\mu$m brightness temperatures suggest the existence of two distinct subgroups which can be represented by the NTrZ and the NEB/SEB. Nevertheless, due to the overlapping range of 5-$\mu$m brightness temperatures between belts and zones, the observed 5-$\mu$m brightness temperatures cannot be used to distinguish belts and zones.

The histogrammed brightness temperatures shown in Figures 3 and 4 suggest that the spectral extremes in terms of 45- and 5-$\mu$m brightness temperatures could be represented with a hot ensemble from the NEB or SEB and the cold ensemble from the NTrZ; however, the degree of overlap between the brightness temperature distributions found in belts and zones suggests that we need to further explore the relation-

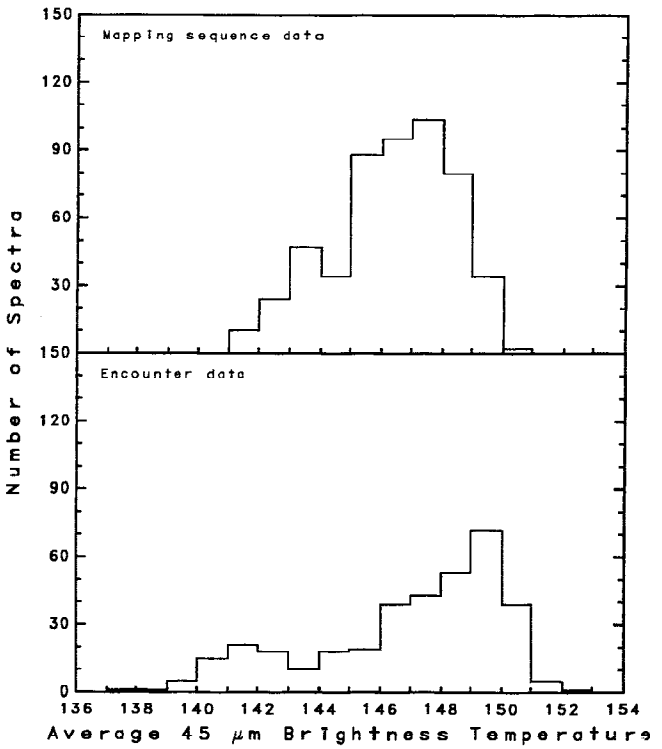


**Figure 3a.** Frequency distributions of observed 45-$\mu$m brightness temperatures for the mapping sequence observations (upper panels) and the higher spatial resolution encounter observations (lower panels).

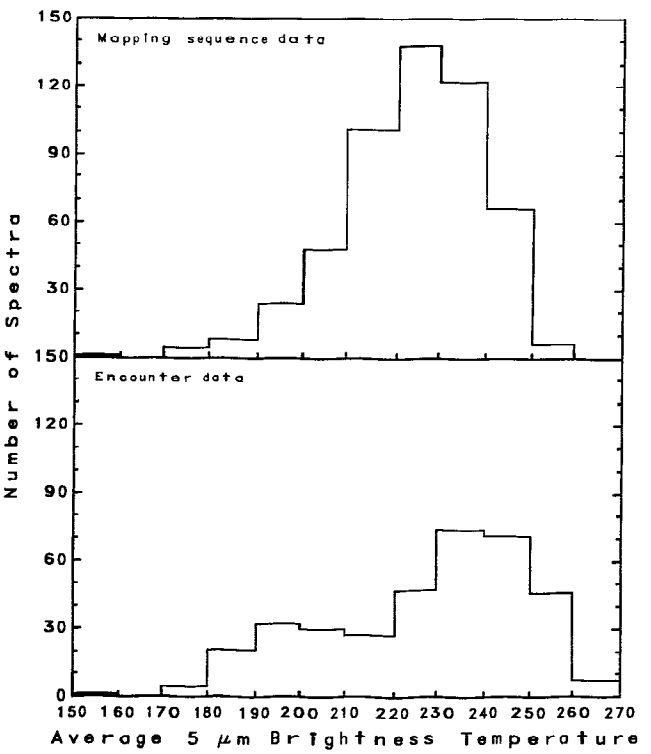


**Figure 3b.** Same as Figure 3a but for the 5-$\mu$m brightness temperatures.

ship between 45- and 5-$\mu$m brightness temperatures. In order to examine this relationship, we have plotted the observed 45-$\mu$m brightness temperatures versus the observed 5-$\mu$m brightness temperatures in Figure 5. Here each character plotted corresponds to an individual IRIS measurement, with the numbers 1–5 corresponding to the different latitude regions. Consistent with the findings of previous investigations [e.g., *Bézard et al.*, 1983], there is a relationship between the observed 45- and 5-$\mu$m brightness temperatures. Starting in the upper right hand corner of the figure, where both $T_{45}$ and $T_5$ are large, we see that most of these observations come from regions 2 and 4, corresponding to the NEB and SEB, respectively (cf. Figure 4). Following the curve toward lower 45- and 5-$\mu$m brightness temperatures, we see that the curve branches and that lower 5-$\mu$m brightness temperatures can either be associated with 45-$\mu$m brightness temperatures in excess of 145 K or less than 144 K. For 5-$\mu$m brightness temperatures less than 220 K, the upper branch is composed primarily of observations from region 3, the EqZ, while the lower branch is composed primarily of observations of region 1, the NTrZ. This branching behavior is consistent with the separation between the EqZ and NTrZ 45-$\mu$m brightness temperatures shown in Figure 4.

The observed relationships between the 45- and 5-$\mu$m brightness temperatures have implications regarding the cloud structure of these regions. Since the radiance in the 45-$\mu$m region of the spectrum originates at pressures less than 1.5 bars, the 45-$\mu$m brightness temperatures are sensitive primarily to changes in the optical depth of the $NH_3$ cloud, while the 5-$\mu$m brightness temperatures contain information primarily on the optical depths of the deeper ($NH_4SH$ and $H_2O$) clouds. Thus, we would expect, based on the relationship of the observed 45- and 5-$\mu$m brightness temperatures, that the optical depths of all three clouds are lowest for the spectra represented by the points in the upper right-hand corner and that the optical depth of the $NH_3$ cloud should increase with decreasing 45-$\mu$m brightness temperature while the optical depths of the $NH_4SH$ and $H_2O$ clouds increase with decreasing 5-$\mu$m brightness temperature. If this is the case, then we need only consider the three extreme spectral ensembles corresponding to the end points of the 45- and 5-$\mu$m relationship shown in Figure 5, namely, spectra that are hot at both 45 and 5 $\mu$m (i.e., upper right end point), spectra that are warm at 45 $\mu$m and cold at 5 $\mu$m (i.e., left end points, upper branch), and spectra that are cold at both 45 and 5 $\mu$m (i.e., left end points, lower branch). All other spectra should have cloud opacity and relative humidity profiles that are intermediate to those retrieved for these spectral ensembles. It is this aspect of the 45- and 5-$\mu$m brightness temperature relationships that we will examine in the remainder of this paper.

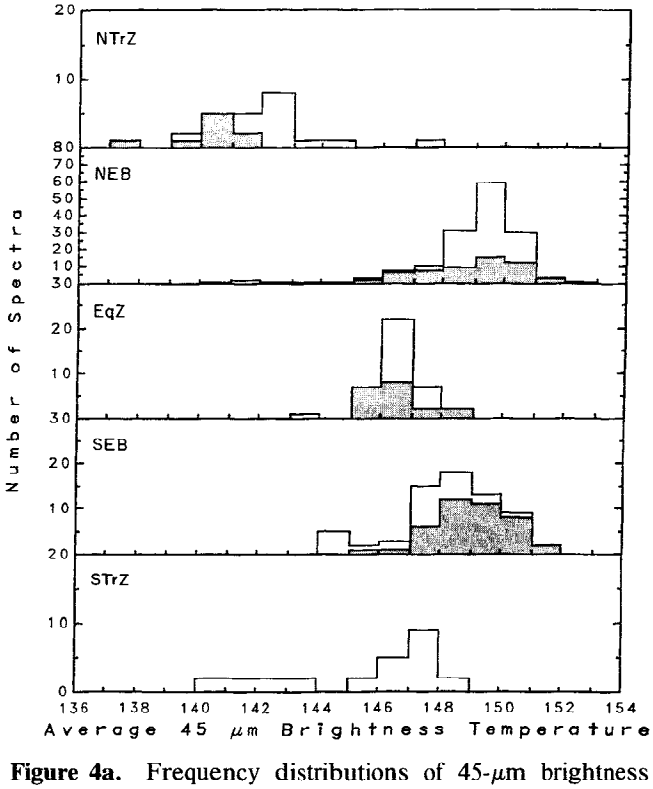


**Figure 4a.** Frequency distributions of 45-$\mu$m brightness temperatures from the spatially resolved encounter observations. The size of the IRIS field of view is less than 5° for all these observations. Shaded portions indicate the distributions for a field of view less than 3°.

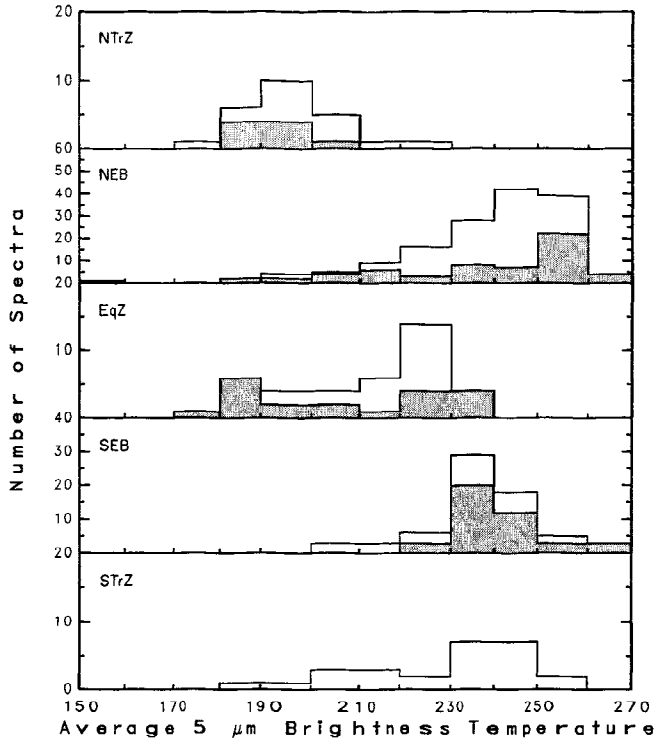


**Figure 4b.** Same as Figure 4a but for 5-$\mu$m brightness temperatures.

## 3. Data Analysis

Our procedure for analyzing the Jovian IRIS spectra is a standard comparison of synthetic and observed spectra. We minimize the "mixing" of different structures by sorting the spectra into homogeneous ensembles based on latitude, emission angle, and 45- and 5-$\mu$m brightness temperature selection criteria (Table 2) that are based on the distribution of observed brightness temperatures previously shown in Figures 4 and 5. Since we are interested in examining the

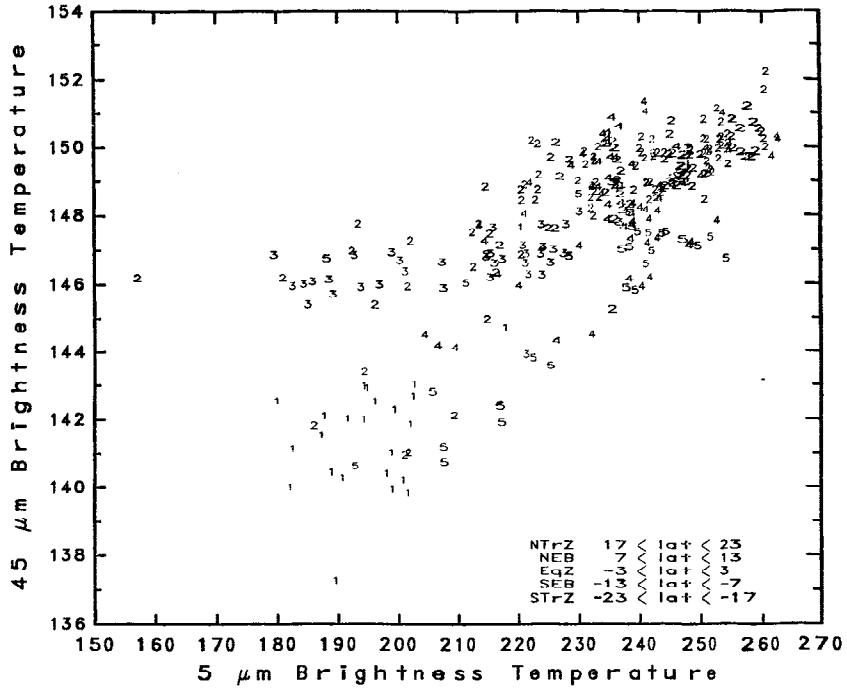


**Figure 5.** Observed 45- and 5-$\mu$m brightness temperature correlation for the NTrZ (1), NEB (2), EqZ (3), SEB (4), and STrZ (5), where the numbers in parentheses correspond to the characters plotted. Each point corresponds to an individual IRIS measurement. The size of the IRIS FOV has been restricted to less than 5°.

average cloud and humidity structure corresponding to each spectral ensemble, we compare our synthetic spectra with the average spectrum corresponding to each ensemble and seek to minimize the difference between the observed and synthetic spectra. However, even at the highest spatial resolution available to IRIS, the Jovian atmosphere is still spatially inhomogeneous; therefore we evaluate the goodness of the model fit and determine the uncertainty (in this case a measure of spatial variability) associated with each parameter using the standard deviation of the individual IRIS spectra comprising a particular ensemble. This variability, due to spatial inhomogeneities (i.e., subpixel variability) and emission angle effects, is generally larger than the instrument noise. With this procedure, the fit to the average IRIS spectrum represents an average cloud structure for that spectral ensemble, though not necessarily the best fit to any of the individual spectra comprising the ensemble.

### 3.1. Modeling Approach

Our approach to the analysis of the IRIS data has several unique aspects. First, we have merged a thermochemical equilibrium model [*Carlson et al.*, 1987] with a radiative transfer model [*Carlson et al.*, 1993]. In the deep atmosphere below their respective condensation levels, condensible species (i.e., $NH_3$, $H_2S$, and $H_2O$) are well mixed, while above their respective condensation levels their abundance follows saturation and a specified relative humidity profile.

To increase the realism/rigor of our radiative transfer analysis, we use the optical properties of $NH_3$, $NH_4SH$, and $H_2O$ to model the spectral dependence of the cloud extinction. Mie theory is used to determine the spectral dependence of the cloud radiative parameters, i.e., the single scattering albedo, $\tilde{\omega}_0$, the phase function asymmetry parameter $g$, and the extinction efficiency factor $Q_{ext}$. For convenience, $Q_{ext}$ is normalized to unity at $\lambda = 0.5$ $\mu$m.

This approach allows us to investigate whether or not thermochemical equilibrium results are consistent with the IRIS observations. The inclusion of chemistry (thermochemical equilibrium and a parameterization of the effects of photochemistry) provides a physical mechanism for the height-dependent mixing ratio profiles. In our analysis, we therefore assume that a mixing ratio profile must be height independent (i.e., uniform) unless there is a known physical mechanism capable of altering it. Finally, by assuming the composition of the clouds, we ensure that the cloud base locations and spectrally dependent cloud extinctions are consistent with the vapor profiles of the condensible species. Moreover, this approach allows us to limit the number of free parameters (e.g., we only have to retrieve a single optical depth per cloud) in our model.

### 3.2. Model Parameters

Our modeling begins with a clear-gas atmosphere (i.e., no cloud) and the gas composition previously determined by *Carlson et al.* [1992a, b, 1993]. Using this initial specification of the gas composition, we retrieve the temperature profile

**Table 2.** Selection Criteria

| Region | Latitude Range, deg | Brightness Temperature, K | |
|---|---|---|---|
| | | 45 $\mu$m | 5 $\mu$m |
| EqZ | −3–3 | $145 \leq T_B \leq 149$ | $180 \leq T_B \leq 205$ |
| NEB | 7–13 | $T_B \geq 149$ | $T_B \geq 250$ |
| NTrZ | 17–23 | $140 \leq T_B \leq 145$ | $180 \leq T_B \leq 205$ |

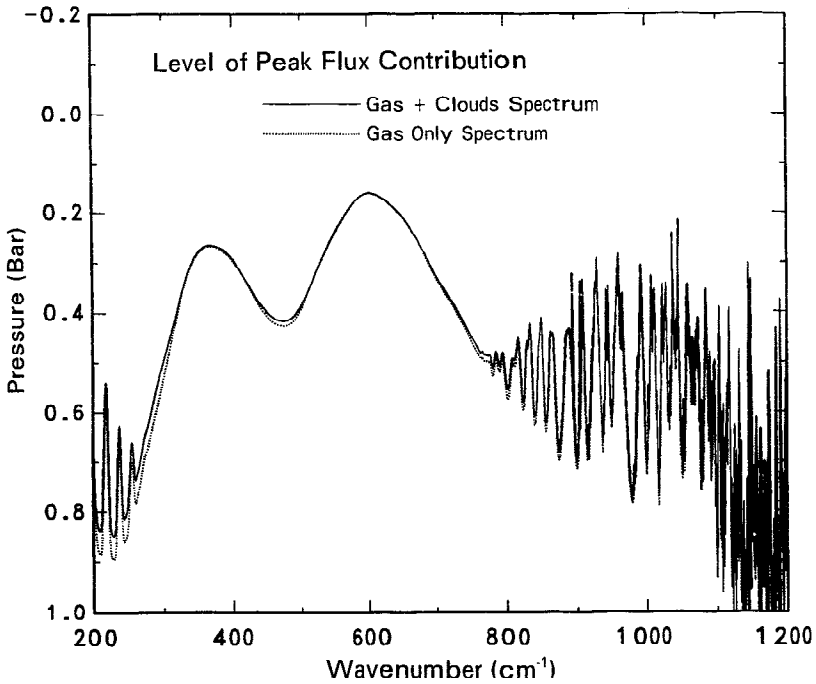


**Figure 6a.** Location of the peak emission level, as determined by a normalized contribution function value of 0.5, calculated with (solid line) and without (dotted line) the inclusion of cloud opacity for the far-infrared regions of the spectrum. In this case, the clouds are optically thin, i.e., our NEB hot spot model.

using a procedure that is similar to the standard inversion process described by *Conrath et al.* [1970]; however, we have replaced the weighting functions with normalized contribution functions. Since the normalized contribution function includes the effects of atmospheric temperature on Planck emission, as well as the multiple scattering effects from the contributing cloud layers, it more accurately depicts the peak emission level than the traditional weighting function approach which is based solely in the distribution of atmospheric gaseous opacity. This results in a small correction to the pressure level of the $\Delta T$ perturbation in the inversion. Nevertheless, the temperature profiles agree to within $\pm 2$ K, the relative accuracy of the inversion.

Figure 6 shows the frequency dependence of the peak

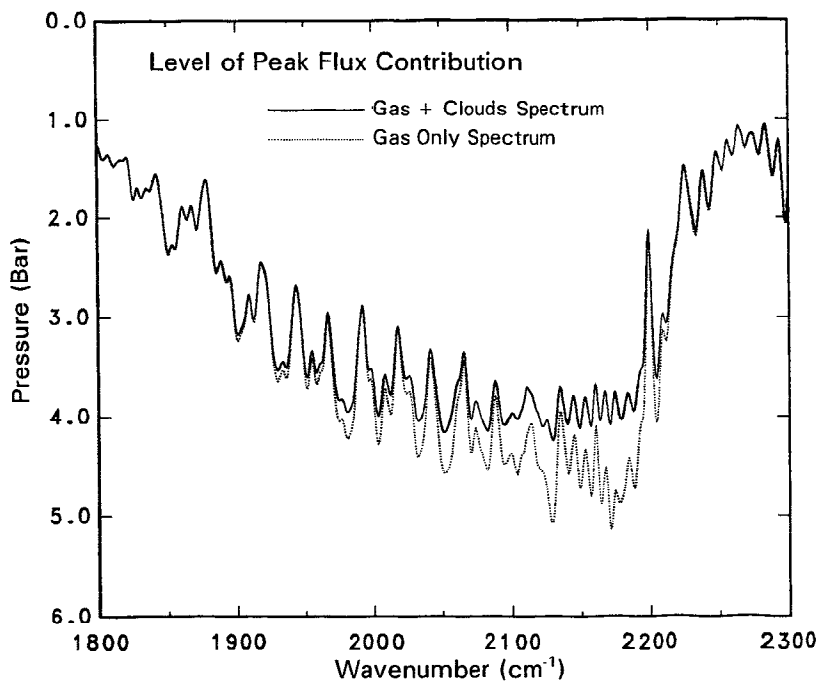


**Figure 6b.** Same as Figure 6a but for the 5-$\mu$m regions of the spectrum.

**Table 3.** Summary of the Model Parameters

| Parameter | Constraints |
|---|---|
| Temperature profile | Retrieved by standard inversion process: 287, 310, 340, 475, 520, 540, 560, 580, 600, 900, 980, 1060, 1098, and 1147 $cm^{-1}$ |
| Gas mixing ratios | |
| $H_2O$ | Above cloud profile: 1950–2100 $cm^{-1}$ region |
| $NH_3$ ($P < 1.5$ bars) | Far-infrared (200–300 and 750–1100 $cm^{-1}$) region |
| $NH_3$ ($P > 1.5$ bars) | 1850–1950 $cm^{-1}$ region |
| $PH_3$ ($P < 1$ bar) | 900–1200 $cm^{-1}$ region |
| $PH_3$ ($P > 1$ bar) | 2100 $cm^{-1}$ region |
| $CH_3D$ | 2050–2350 $cm^{-1}$ |
| $GeH_4$ | 2111 $cm^{-1}$ |
| Hydrogen para fraction profile | Differential absorption strength from line center to line wing in the 300–700 $cm^{-1}$ region |
| Cloud base locations | |
| $NH_3$ | Based on $NH_3$ profile (thermochemical model) |
| $NH_4SH$ | $NH_3$ profile; need for additional opacity near 2 bars |
| $H_2O$ | Based on water profile (thermochemical model) |
| Cloud optical depths | |
| $NH_3$ | Far-infrared spectrum, 200–300 $cm^{-1}$ region |
| $NH_4SH$ | Continuum level 1900–2150 $cm^{-1}$ |
| $H_2O$ | Continuum level 2150–2250 $cm^{-1}$ |
| Effective radius | |
| $NH_3$ cloud | Dependence of cloud extinction from 200 to 2300 $cm^{-1}$ |
| $NH_4SH$ cloud | Assumed to be 3 $\mu$m (not retrieved) |
| $H_2O$ cloud | Assumed to be 10 $\mu$m (not retrieved) |
| $H_p/H_g$ | |
| $NH_3$ cloud | Continuum level 360–520 $cm^{-1}$ |
| $NH_4SH$ cloud | 1100–1200 $cm^{-1}$ continuum; 1800–1950 $cm^{-1}$ region |
| $H_2O$ cloud | Shape of 1900–2250 $cm^{-1}$ continuum |
| Vapor scale heights | |
| $NH_3$ | 200–300 and 900–1100 $cm^{-1}$ regions |
| $PH_3$ | 900–1000 $cm^{-1}$ region |

emission level calculated with (solid line) and without (dashed line) the inclusion of cloud opacity. We define the location of the peak emission level to be the pressure at which the normalized contribution function has a value of 0.5. Thus, half of the radiation originates above this level and half originates below this level. As can be seen from the comparison with and without the inclusion of cloud opacity curves shown in Figure 6, the effect that the inclusion of cloud opacity has is spectrally dependent. We are able to use this differing sensitivity to the presence of clouds to separate cloud and temperature effects. Moreover, by modeling the spectral dependence of cloud extinction using the optical properties of the condensate, the spectral dependence of cloud extinction is no longer a free parameter which limits the continuum opacity sources.

An initial thermal profile, supplied by B. J. Conrath (personal communication, 1986) provides the starting point for our inversion algorithm. This profile is iteratively adjusted until the synthetic and observed spectra agree to within the noise equivalent radiance of the average IRIS spectrum at selected wavenumbers within the 200–1200 $cm^{-1}$ interval, where cloud effects are weakest. The specific frequencies used are 287, 310, 340, 475, 520, 540, 560, 580, 600, 900, 980, 1060, 1098, and 1147 $cm^{-1}$. As in previous analyses [e.g., *Kunde et al.*, 1982], at pressures greater than 1 bar, we have initially extrapolated the profile with an adiabatic lapse rate calculated for a hydrogen mole fraction of 0.88 and a helium mole fraction of 0.12 [*Gautier et al.*, 1981] and taking into account the variation of specific heat with temperature. We have also examined the temperature profile in the deep atmosphere by inverting the 5-$\mu$m measurements where possible.

The need for an iterative approach is evident in Figure 6, which shows that the inclusion of cloud opacity alters the location of the peak emission level. The degree to which the outgoing radiation is affected by the presence of clouds depends on the location of the peak emission level relative to the cloud and, of course, on the optical depth of the cloud.

With this initial temperature profile, we then analyze the far-infrared IRIS measurements to determine the gas composition of the upper troposphere. Once this gas composition has been constrained, we then retrieve the optical depth of the $NH_3$ cloud as well as the vertical distribution of $NH_3$ cloud extinction.

At this point, we then reexamine the temperature profile and gas composition of the upper troposphere with an emphasis on the height-dependent gas profiles. Once we have constrained the gas and cloud properties in the upper troposphere, we turn our attention to the 5-$\mu$m IRIS observations and retrieve the gas composition and cloud structure of the deeper atmosphere.

The free parameters in our model are summarized in Table 3. Some parameters that are necessary for our radiative transfer calculations cannot be retrieved from the IRIS measurements. Figure 7 shows the spectral dependence of $Q_{ext}$ as a function of particle size for $NH_3$ in the far infrared

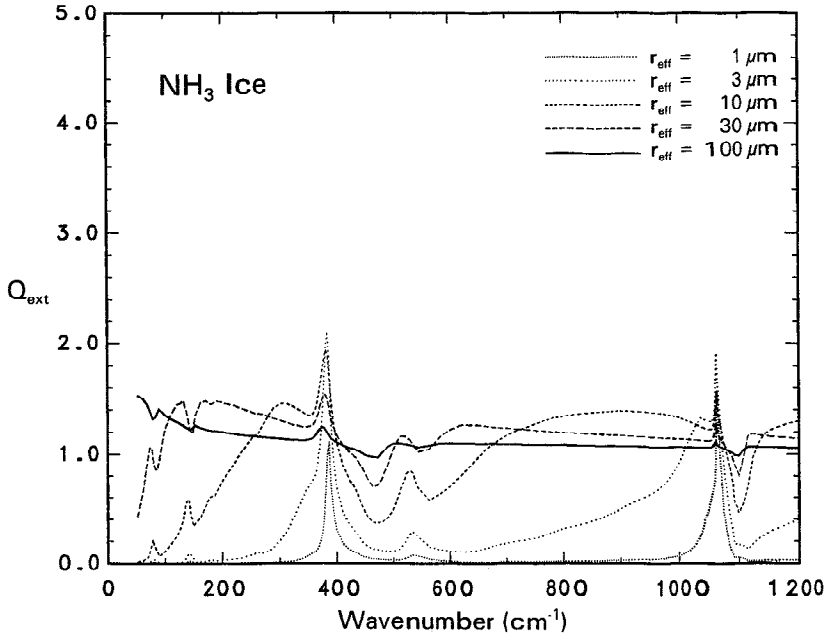


**Figure 7a.** Spectral dependence of $Q_{ext}$ as a function of particle size for $NH_3$ in the far infrared.

(Figure 7a), $NH_3$ in the 5-$\mu$m region (Figure 7b), $NH_4SH$ in the 5-$\mu$m region (Figure 7c), and water in the 5-$\mu$m region (Figure 7d). In our calculations, $Q_{ext}$ is normalized to unity at $\lambda = 0.55$ $\mu$m. For each cloud, we retrieve $\tau_{ref}$ the optical depth referenced at $\lambda = 0.55$ $\mu$m. At any frequency, the monochromatic cloud particle optical depth is simply the product of $\tau_{ref}$ and the value of $Q_{ext}$ at that frequency.

In order to retrieve the effective radius of the cloud particles, the particle size dependence of the extinction optical depth must change with frequency. As can be seen from the comparison of Figures 7a and 7b, for $NH_3$, the value of $Q_{ext}$ changes by nearly an order of magnitude as a function of particle size. This particle size dependence at a given frequency combined with the broad spectral coverage of the IRIS measurements, their sensitivity to the $NH_3$ cloud, and the near order of magnitude variation in the value of $Q_{ext}$ for small particles from 200 $cm^{-1}$ to 2000 $cm^{-1}$ allows us to retrieve the effective radius of the $NH_3$ cloud. However, the situation is different for $NH_4SH$ and $H_2O$, where as shown in Figures 7c and 7d, the spectral variation of $Q_{ext}$ is not a strong function of particle size or frequency. For these clouds, we are forced to assume the effective radius of the cloud particle size distribution. In this case, we have assumed that the $NH_4SH$ and $H_2O$ clouds are composed of particles with effective radii of 3 $\mu$m and 10 $\mu$m, respectively. A different particle size assumption would

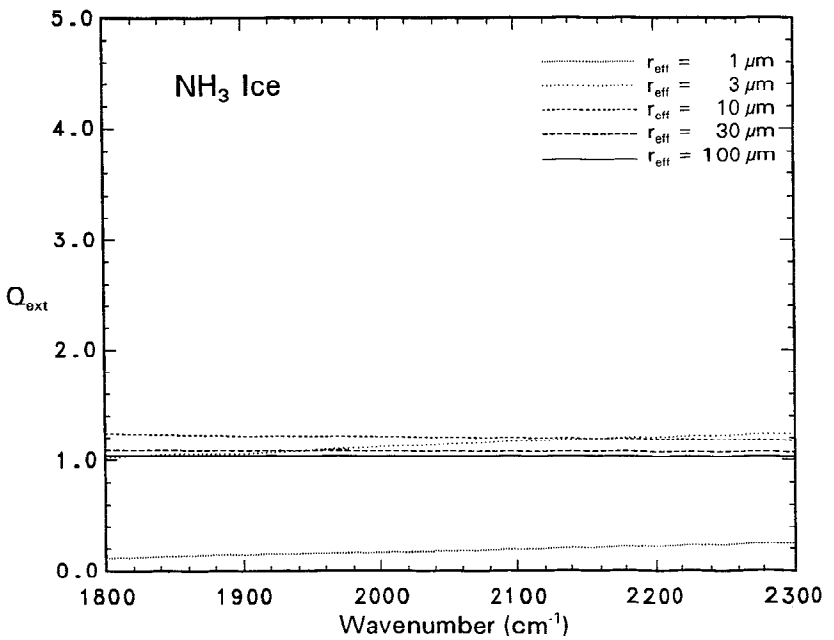


**Figure 7b.** Same as Figure 7a but for $NH_3$ in the 5-$\mu$m region.

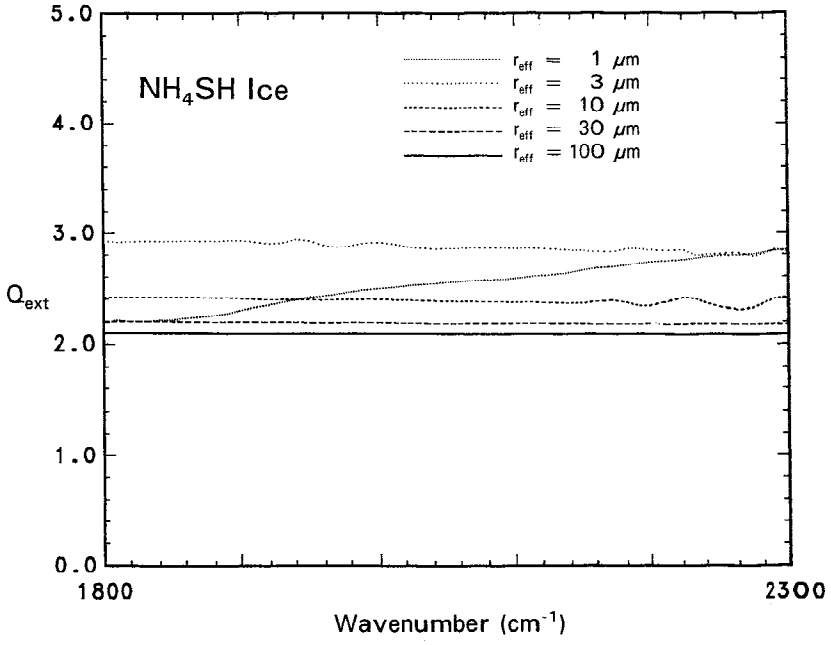


**Figure 7c.** Same as Figure 7a but for $NH_4SH$ in the 5-$\mu$m region.

result in a different phase function and would only require the value of $\tau_{ref}$ to be scaled, but the radiative extinction would be the same. Thus, given our particle size assumptions, we can retrieve the optical depth of the $NH_4SH$ and/or $H_2O$ cloud, but this specific value of the optical depth is only meaningful in the context of our particle size assumption.

The importance of scattering in the 5-$\mu$m spectral region is illustrated by the values of the single scattering albedo for $NH_3$, $NH_4SH$, and $H_2O$ (Figure 7e) cloud particles. In all cases the single scattering albedos are significantly larger than zero and the asymmetry parameters (not shown) are larger than ~0.7, which means that, due to forward scattering, even at relatively large optical depths (e.g., $\tau \approx 5$) a significant fraction of the radiation is diffusely transmitted through these clouds. Thus it is important to correctly model the spectral dependence of cloud extinction and include scattering.

### 3.3. Spectral Sensitivity to Model/Retrieved Parameters

In this section we illustrate both the iterative nature of our modeling approach and the sensitivity of the synthetic spectra to various model parameters. We remind the reader that greater detail can be found in the work by *Carlson et al.* [1992a, b, 1993]; moreover, we emphasize the illustrative nature of some of our figures. Finally, while in this paper we are primarily interested in variations in the cloud structure,

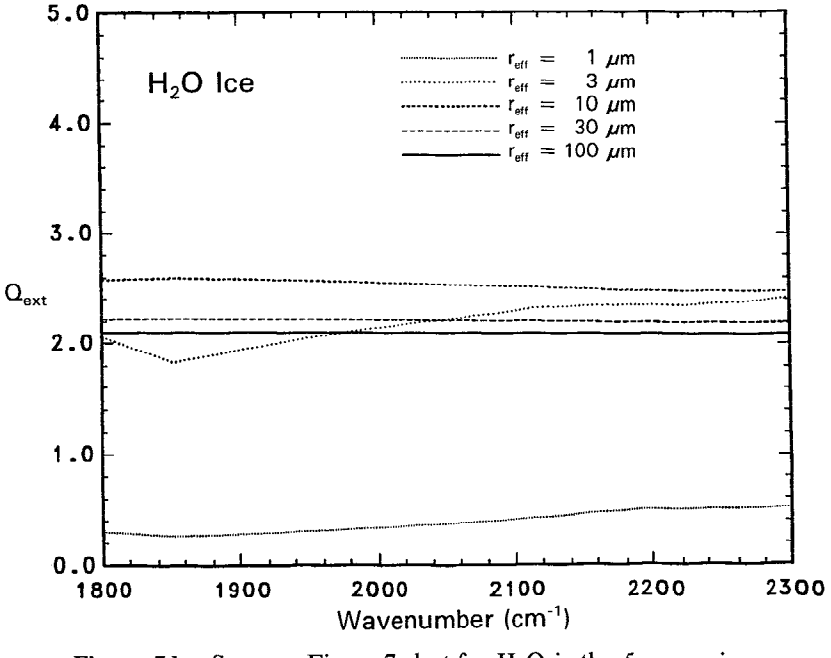


**Figure 7d.** Same as Figure 7a but for $H_2O$ in the 5-$\mu$m region.

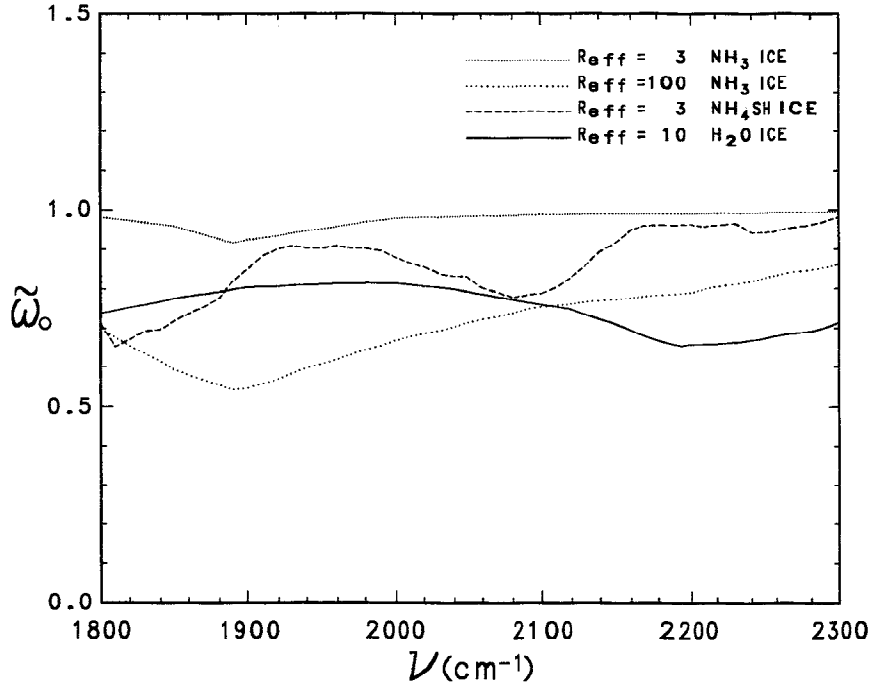


**Figure 7e.** Spectral dependence of $\tilde{\omega}_0$ as a function of particle size for the $NH_3$, $NH_4SH$, and $H_2O$ cloud particles in the 5-$\mu$m region.

i.e., variations in continuum opacity sources, it is necessary to briefly consider gaseous opacity with an emphasis on the differences between our results and those obtained by previous investigators.

The first step in modeling the IRIS spectra is the calculation of clear-gas synthetic spectra. In order to illustrate the importance of the opacity provided by $H_2$ and $NH_3$ in determining the shape of the spectrum, we compare synthetic spectra calculated with only $H_2$ opacity (solid line) in Figure 8, with $H_2$ and $NH_3$ opacity (dashed line), and with all of the far-infrared gaseous opacity sources (dash-dot line) to the average IRIS NEB hot spot spectrum (dotted line). As in all of our subsequent comparisons, the standard deviation of the individual spectra comprising the average is plotted in the lower portion of the figure, using the right-hand scale, along with the difference between the synthetic and observed spectra.

This comparison shows that most of the high-frequency spectral variability in the far-infrared region of IRIS spectra is due to absorption by $NH_3$. While $PH_3$ and $CH_3D$ absorb throughout the 900–1200 $cm^{-1}$ region, their impact on the spectrum is most pronounced in the 1100–1200 $cm^{-1}$ interval.

The sensitivity of the far infrared to hydrogen absorption is further detailed in Figure 9, which compares synthetic spectra calculated with height-independent (i.e., constant) para fractions of 0.25, 0.27, 0.30, and 0.35. This comparison illustrates that it is the 300–520 $cm^{-1}$ interval that is primarily sensitive to the ratio of ortho-to-para hydrogen. In this case a para fraction of 0.3 provides the closest fit to the IRIS observations.

In both Figures 8 and 9 the continuum level in the 200–300 $cm^{-1}$ region of the spectrum is poorly fit. Since this spectral interval is sensitive to the abundance and profile of $NH_3$, let us first consider an artificial case, namely, that of a height-independent $NH_3$ profile. Figure 10 compares the spectrum calculated with our best fit height-dependent $NH_3$ profile (solid line) with spectra calculated assuming height-independent $NH_3$ mixing ratios of $8.9 \times 10^{-5}$ (dashed line) and $1.78 \times 10^{-4}$ (solar, dash-dot line). The average IRIS NEB hot spot spectrum (dotted line) is also shown. Clearly, the height-independent $NH_3$ profiles provide too much opacity in the 800–1150 $cm^{-1}$ region as well as in the $NH_3$ line centers in the 200–300 $cm^{-1}$ region. From this, we conclude that the mixing ratio of $NH_3$ must be less than $8.9 \times 10^{-5}$ in the upper troposphere.

In addition, as shown in Figure 7 of *Kunde et al.* [1982], a saturated (i.e., 100% relative humidity) $NH_3$ profile also provides too much opacity in the 800–1150 $cm^{-1}$ region. Based on this result, we conclude, as did Kunde et al., that the $NH_3$ profile is subsaturated. In fact, at pressures less than 0.6 bar, our retrieved, height-dependent $NH_3$ profile (solid line in Figure 10) is in agreement with that determined by Kunde et al. However, Kunde et al. assumed, based on their poor fit in the 200–300 $cm^{-1}$ region, that the mole fraction of $NH_3$ increases from $3.0 \times 10^{-5}$ at 0.6 bar to a solar value of $1.78 \times 10^{-4}$ at 1 bar. Furthermore, they assumed that the $NH_3$ abundance at the 1-bar level is well mixed. We, on the other hand, do not assume that the abundance of $NH_3$ increases to the solar value at 1 bar, nor do we assume that the 1-bar value is representative of the well-mixed abundance, since $NH_3$ is consumed in the formation of $NH_4SH$. Finally, as shown by the spectra (that were calculated with height-independent $NH_3$ profiles) in Figure 10, a solar abundance of $NH_3$ (dash-dot line) still does not provide an acceptable continuum fit to the IRIS measurements in the 200–300 $cm^{-1}$ region (i.e., additional opacity is still required).

In modeling the gaseous opacity, line shapes are modeled using a Voigt profile. However, to account for the sub-Lorentzian behavior of the far wings, we have adopted the common expedient of truncating the Lorentz profile 50 $cm^{-1}$

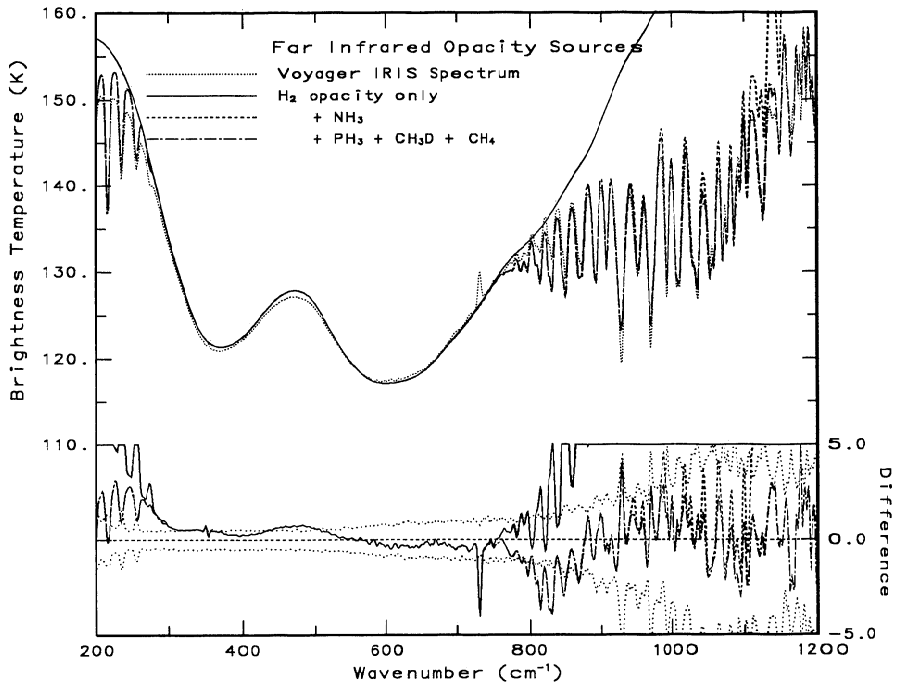


**Figure 8.** Comparison of the average IRIS NEB hot spot spectrum (dotted line) to synthetic spectra calculated with only $H_2$ opacity (solid line), $H_2$ and $NH_3$ opacity (dashed line), and with all known gaseous sources of opacity (dash-dot line). In this case the dash-dot line lies close to the dotted line in the upper portion of the figure and is perhaps more easily seen in the difference portion. The difference between the synthetic and observed spectra is plotted in the lower portion of the figure along with the standard deviation of the individual IRIS spectra comprising this ensemble (dotted lines).

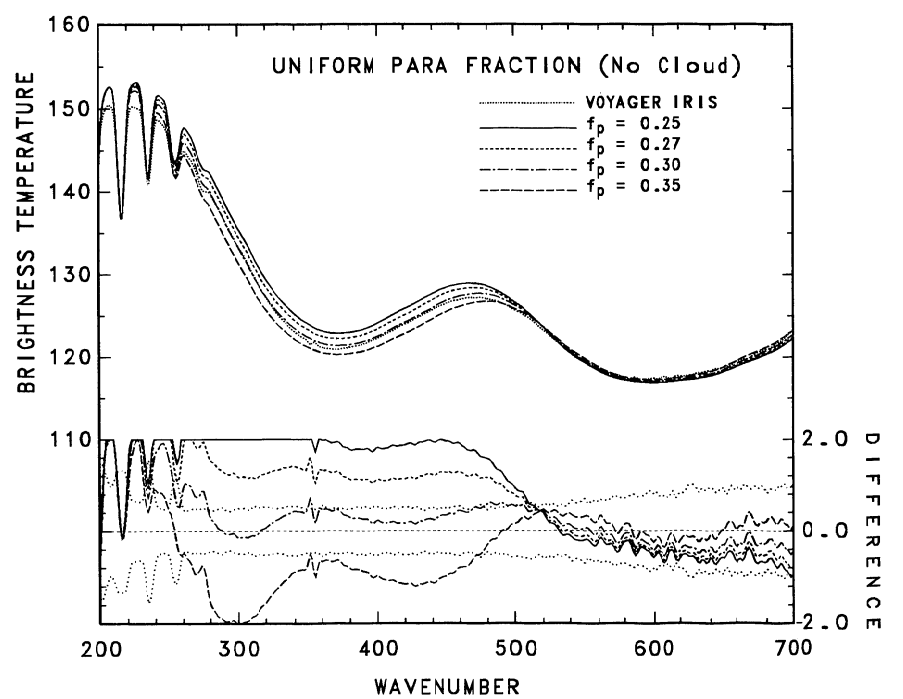


**Figure 9.** Illustration of the sensitivity of the far-infrared, 200–700 $cm^{-1}$ spectral interval to variations of a height-independent para hydrogen fraction. Synthetic spectra are calculated without cloud opacity for uniform (height-independent) para fractions of 0.25 (solid line), 0.27 (short-dashed line), 0.30 (dash-dot line), and 0.35 (long-dashed line). The average IRIS NEB hot spot spectrum is also shown (dotted line). The difference between the synthetic and observed spectra is plotted in the lower portion of the figure.

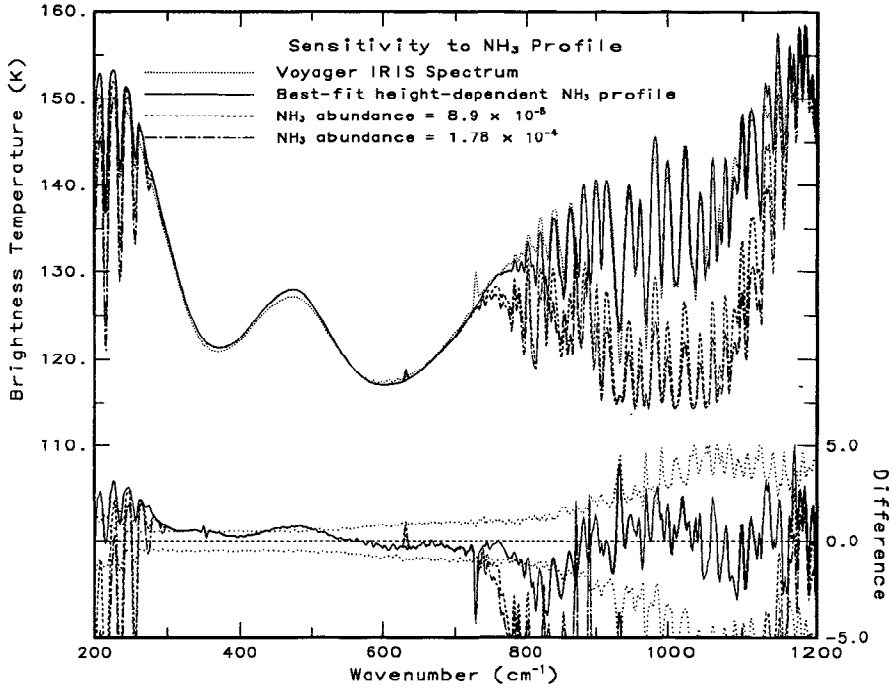


**Figure 10.** Comparison of synthetic spectra calculated with our best fit height-dependent $NH_3$ profile (solid line), a height-independent $NH_3$ profile with an $NH_3$ mixing ratio of $8.9 \times 10^{-5}$ (dashed line), and a height-independent $NH_3$ profile with an $NH_3$ mixing ratio of $1.78 \times 10^{-4}$ (dash-dot line) and the average IRIS NEB hot spot spectrum (dotted line).

from the center of each line. Thus, uncertainties in the far-wing treatment complicate the situation, but as shown in Figure 11 the difference among the synthetic spectra calculated with different values for the Lorentz cut-off, are relatively small in the 200–300 $cm^{-1}$ region and unlikely to be sufficient to account for the discrepancy between the synthetic and observed spectra.

We know, from the results shown above, that additional

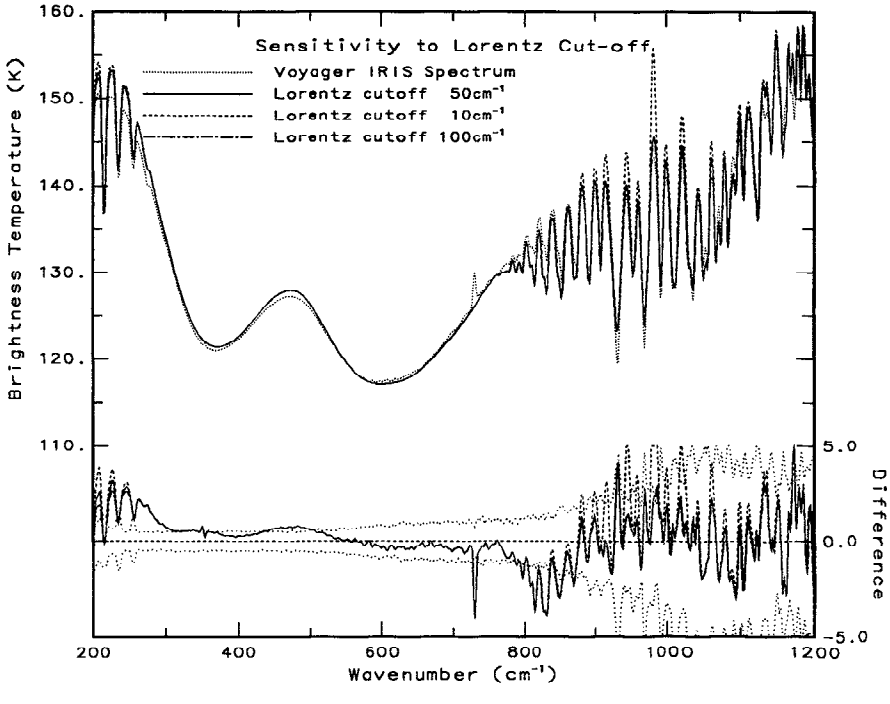


**Figure 11.** Sensitivity of the synthetic spectra to the treatment of the sub-Lorentzian behavior of the far wings. Comparison of synthetic spectra calculated with Lorentz cutoffs of 50 $cm^{-1}$ (solid line), 10 $cm^{-1}$ (dashed line), and 100 $cm^{-1}$ (dash-dot line) with the average IRIS NEB hot spot spectrum (dotted line).

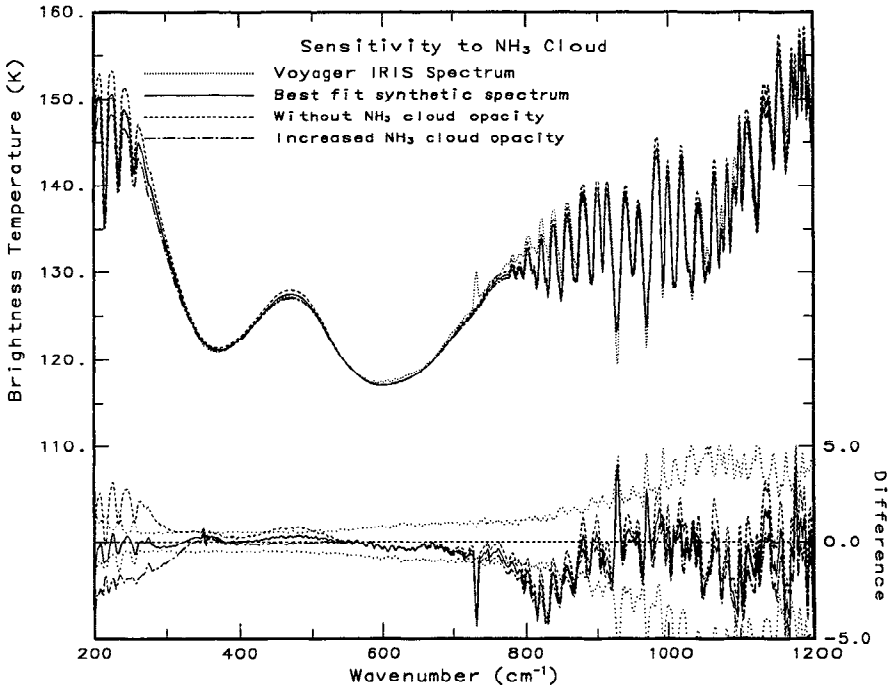


**Figure 12.** Sensitivity of the synthetic spectra to the optical depth of the $NH_3$ cloud. Comparison of our best fit synthetic spectrum calculated with an $NH_3$ cloud optical depth of 0.27 (solid line) with spectra calculated without the inclusion of $NH_3$ cloud opacity (dashed line) and with increased $NH_3$ cloud opacity ($\tau$ = 0.37, dash-dot line) to the average IRIS NEB hot spot spectrum (dotted line).

opacity is required in the 200–300 $cm^{-1}$ region of the spectrum and that this opacity cannot be provided by gaseous absorption. The only remaining far infrared opacity source is the $NH_3$ cloud. By including spectrally dependent $NH_3$ cloud extinction consistent with their $NH_3$ vapor profile, *Kunde et al.* [1982] would also have been able to simultaneously fit both the 200–300 and 800–1150 $cm^{-1}$ regions of the spectrum with a single $NH_3$ profile.

The sensitivity of the spectrum to the optical depth of the $NH_3$ cloud is shown in Figure 12. In our best fit spectrum (solid line) the optical depth of the $NH_3$ cloud is 0.27. Increasing the optical depth of the cloud to 0.37 (dash-dot line) results in too much cloud opacity, while removing the cloud (dashed line) results in a poor continuum fit in the 200–300 $cm^{-1}$ region. Comparison between the spectra calculated with (solid and dash-dot lines) and without (dashed line) the inclusion of $NH_3$ cloud extinction illustrates the effect of spectrally dependent $NH_3$ cloud extinction on the IR spectrum.

Once $NH_3$ cloud opacity has been included, we have to reexamine the gas profiles. In particular, since $NH_3$ cloud extinction alters the continuum in the low-frequency wing of the S(0) hydrogen line, we have to reexamine the para hydrogen profile. Figure 13 shows a comparison between synthetic spectra calculated with height-independent para fraction values of 0.25, 0.27, 0.30, and 0.35 and the average IRIS NEB hot spot spectrum (dotted line). Once spectrally dependent cloud extinction is included, a more complicated para fraction profile is required (see *Carlson et al.* [1992b] for a more detailed discussion). Radiation in the centers of the S(0) and S(1) hydrogen lines is relatively insensitive to the presence of the $NH_3$ cloud. At these frequencies a para fraction of 0.3 still provides the closest fit. However, radiation in the wing of the S(0) line near 300 $cm^{-1}$, which originates from deeper levels, is substantially affected by $NH_3$ cloud absorption. Here a para fraction of 0.27 provides the best fit to the IRIS observations. Based on this shift in para fraction with the change in depth of the peak emission level from the S(0) line center to the wing (as illustrated in Figure 6), we conclude that a height-dependent para fraction profile is required. That the S(1) hydrogen line is sensitive to the same altitude range (see Figure 6) but relatively insensitive to the para fraction allows us to separate the para hydrogen and temperature profile effects.

With the inclusion of spectrally dependent $NH_3$ cloud extinction, we can now reexamine the height dependence of the $NH_3$ vapor profile. Figure 14 shows a comparison between synthetic spectra calculated with our best fit $NH_3$ profile, in which the mixing ratio below the $NH_3$ cloud and above the 1 bar level is $3.0 \times 10^{-5}$ (solid line), with spectra calculated assuming that the $NH_3$ mixing ratio increases to $8.9 \times 10^{-5}$ (dashed line), and $1.78 \times 10^{-4}$ (dash-dot line) at 1 bar. The average IRIS NEB hot spot spectrum (dotted line) is also shown. From this comparison, we can see that the *Kunde et al.* [1982] assumption of a mole fraction that increases to the solar abundance at 1 bar is precluded by the IRIS observation. Thus, in our best fit profile, the $NH_3$ mixing ratio at the 1-bar level is $3.0 \times 10^{-5}$, above which it is constant until the saturation level, which occurs near 0.5 bar, above which the profile is subsaturated.

The final model parameter to be constrained by the far-infrared measurements is the particle-to-gas scale height ratio for the $NH_3$ cloud, which determines the vertical distribution of the $NH_3$ cloud opacity. Figure 15 shows a comparison between synthetic spectra calculated with $H_p/H_g$ = 0.15 (solid line), 0.05 (dashed line), 0.25 (dash-dot

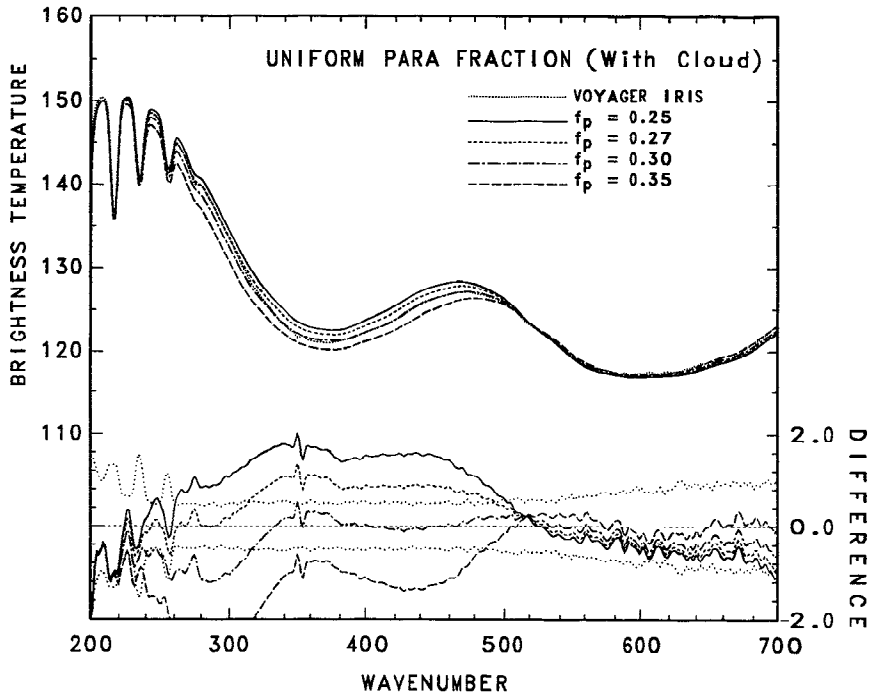


**Figure 13.** Comparison of synthetic spectra calculated with the inclusion of $NH_3$ cloud opacity and height-independent para fractions of 0.25 (solid line), 0.27 (short-dashed line), 0.30 (dash-dot line), and 0.35 (long-dashed line) with the average IRIS NEB hot spot spectrum (dotted line).

line) and the average IRIS NEB hot spot spectrum (dotted line). As shown, the spectra are less sensitive to the vertical distribution of cloud opacity ($H_p/H_g$) than they are to the total optical depth of the cloud (shown in Figure 12). In this case, since the optical depth of the $NH_3$ cloud is small, all three spectra provide an acceptable fit to the IRIS observations. Nevertheless, the difference between the synthetic and observed spectra is minimized with $H_p/H_g$ = 0.15 and

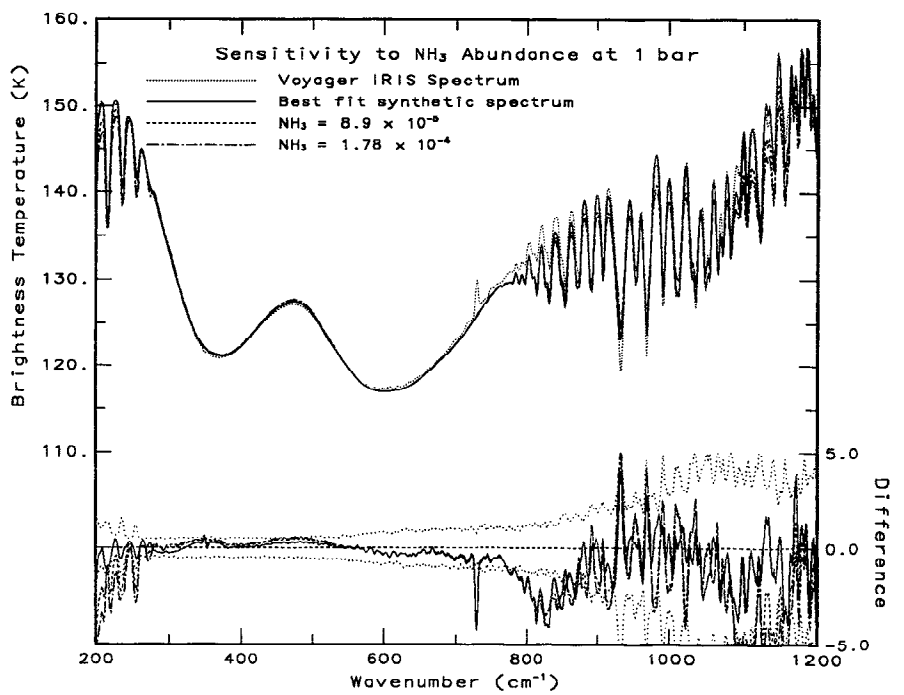


**Figure 14.** Sensitivity of the synthetic spectra to the $NH_3$ mixing ratio at 1 bar. Comparison between synthetic spectra calculated with the same vapor profile above 0.5 bar, but with 1-bar $NH_3$ mixing ratios of $3.0 \times 10^{-5}$ (solid line), $8.9 \times 10^{-5}$ (dashed line), and $1.78 \times 10^{-4}$ (dash-dot line) with the average IRIS NEB hot spot spectrum (dotted line).

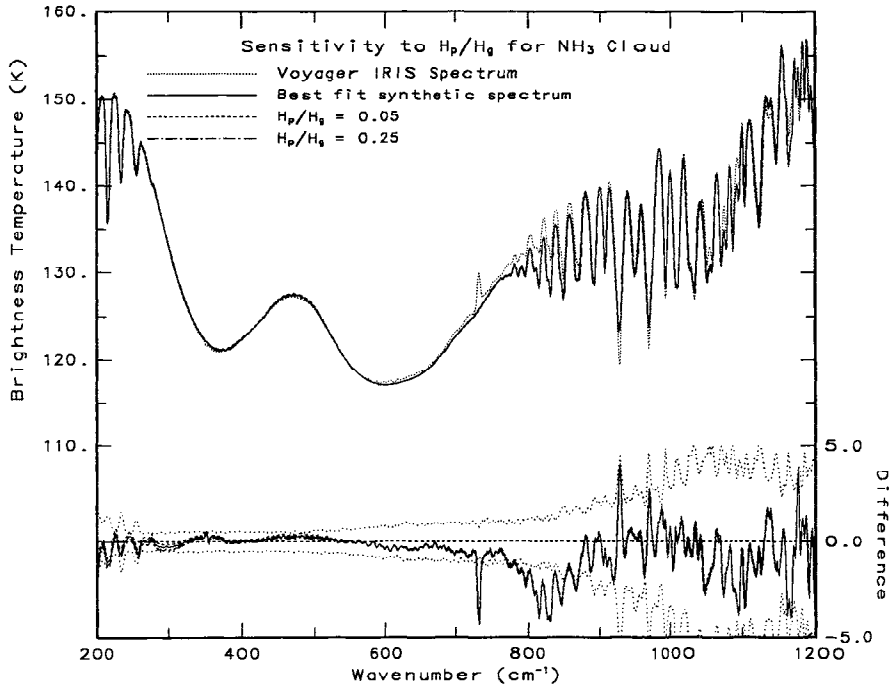


**Figure 15.** Sensitivity of the synthetic spectra to the vertical distribution of $NH_3$ cloud opacity. Comparison of synthetic spectra calculated with particle-to-gas scale height ratios of 0.15 (solid line), 0.05 (dashed line), and 0.25 (dash-dot line) with the average IRIS NEB hot spot spectrum (dotted line).

the data do provide sufficient constraints to rule out values in excess of 0.25, suggesting that the $NH_3$ cloud is physically thin and therefore more like terrestrial cirrus than cumulus, consistent with the microphysical modeling results of *Carlson et al.* [1988].

With the gas composition and $NH_3$ cloud properties constrained, we can now turn our attention to the 5-$\mu$m region of the spectrum. In the discussion above, we have ignored the effective radius of the $NH_3$ cloud particles, since this parameter is constrained by the spectral dependence of $NH_3$ cloud extinction from 200 to 2300 $cm^{-1}$. In this investigation we have assumed that the particle size distribution can be modeled using a modified gamma distribution [*Hansen and Travis*, 1974] with an effective variance of 0.25. The value 0.25 was chosen as representative of a cirrus (i.e., ice cloud) distribution based on terrestrial analogs. As previously shown in Figure 7, for small particles, the normalized value of $Q_{ext}$ increases by nearly an order of magnitude from the far infrared to the 5-$\mu$m region, while for large particles, $Q_{ext}$ is spectrally flat. The difference in the value of $Q_{ext}$ between small and large particles in the far infrared means that in order to provide the same amount of opacity the reference optical depth of the small particles has to be nearly an order of magnitude larger than that of the large particles. Thus, both $\tau = 0.27$ of 100-$\mu$m particles and $\tau = 2.0$ of 3-$\mu$m particles provide a good fit to the continuum in the 200–300 $cm^{-1}$ region. However, in the 5-$\mu$m region, where the values of $Q_{ext}$ are comparable for both small and large particles, the small-particle $NH_3$ cloud provides nearly an order of magnitude more extinction than the large-particle cloud. The impact that this has on the spectrum is shown in Figure 16, which compares synthetic spectra calculated with $\tau = 0.27$ of 100-$\mu$m particles (solid line), $\tau = 2.0$ of 3-$\mu$m particles (dashed line), and the average IRIS NEB hot spot spectrum (dotted line). The small-particle cloud provides too much opacity in the 5-$\mu$m region. Therefore we conclude that the $NH_3$ cloud is composed primarily of large particles.

Figure 17a shows the water vapor (solid line) opacity throughout this spectral interval, which dominates the spectrum from 1930 to 2050 $cm^{-1}$. The addition of $NH_3$ (dashed line, which is overlapped by the dash-dot line in the 1800–1900 $cm^{-1}$ region) improves the fit in the 1800–1900 $cm^{-1}$ region of the spectrum, but has little impact at frequencies larger than 2100 $cm^{-1}$. Including the opacity provided by $PH_3$ (dash-dot line in Figure 17a; solid line in Figure 17b) improves the agreement between the synthetic and observed spectra in the 2025–2125 and 2200–2300 $cm^{-1}$ regions of the spectrum. The addition of $CH_3D$ improves the fit in the 2075–2225 $cm^{-1}$ region. The other gases, $CH_4$, $GeH_4$, and CO (dash-dot line) have smaller effects on the spectrum.

While there is general agreement between the observed and synthetic spectra in terms of the locations of the absorption features, the overall continuum level as well as the depths of the absorption features are still poorly fit. In addition, the 2100–2200 $cm^{-1}$ continuum level is too high. Increasing the abundance of $CH_3D$ would lower the continuum level here, but it would also impact the continuum level in the 1100–1200 $cm^{-1}$ region of the spectrum, resulting in an unacceptable fit.

An additional source of opacity is required in order to obtain an acceptable fit to the continuum level in the 2150–2200 $cm^{-1}$ region of the spectrum. Figure 18 compares synthetic spectra calculated with a saturated water profile with (solid line) and without (dashed line) the inclusion of spectrally dependent water cloud extinction. Based on this comparison, we see that the presence of the water cloud influences the spectrum throughout the 1950–2200 $cm^{-1}$ region. More important, we see that the addition of water

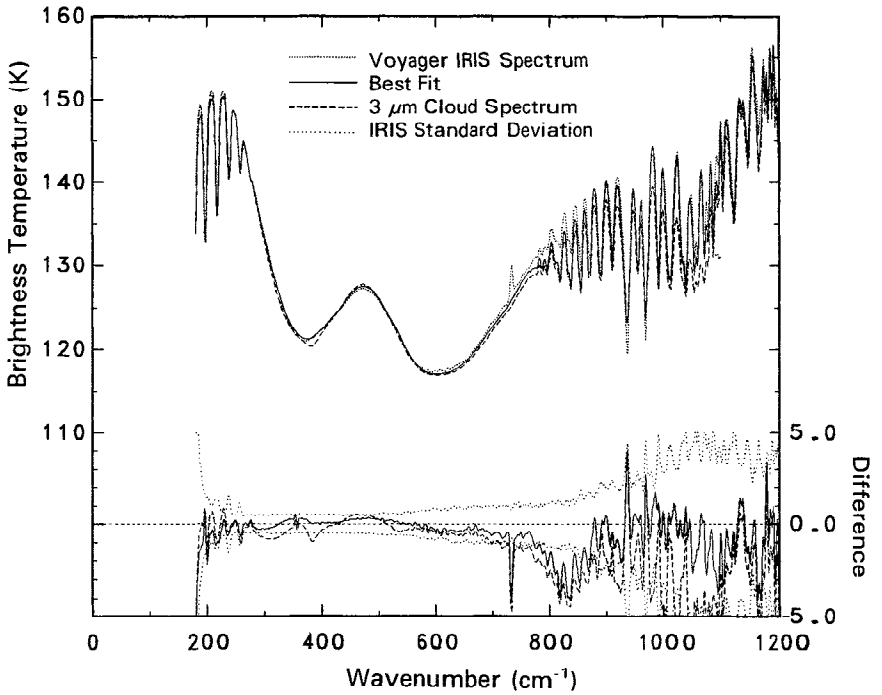


**Figure 16a.** Illustration of the spectral sensitivity to the effective radius of the $NH_3$ cloud particles. Comparison of synthetic spectra calculated with an effective radius of 100 $\mu$m and $\tau = 0.27$ (solid line) and an effective particle radius of 3 $\mu$m and $\tau = 2$ (dashed line) with the average IRIS NEB hot spot spectrum (dotted line). The optical depth of the $NH_3$ cloud was constrained to provide an acceptable fit, i.e., the difference between the synthetic and observed spectra is less than the standard deviation of the individual NEB hot spot spectra in the 200–300 $cm^{-1}$ continuum region. While small particles provide an almost acceptable fit to the far-infrared region, they clearly provide too much opacity in the 5-$\mu$m region (Figure 16b).

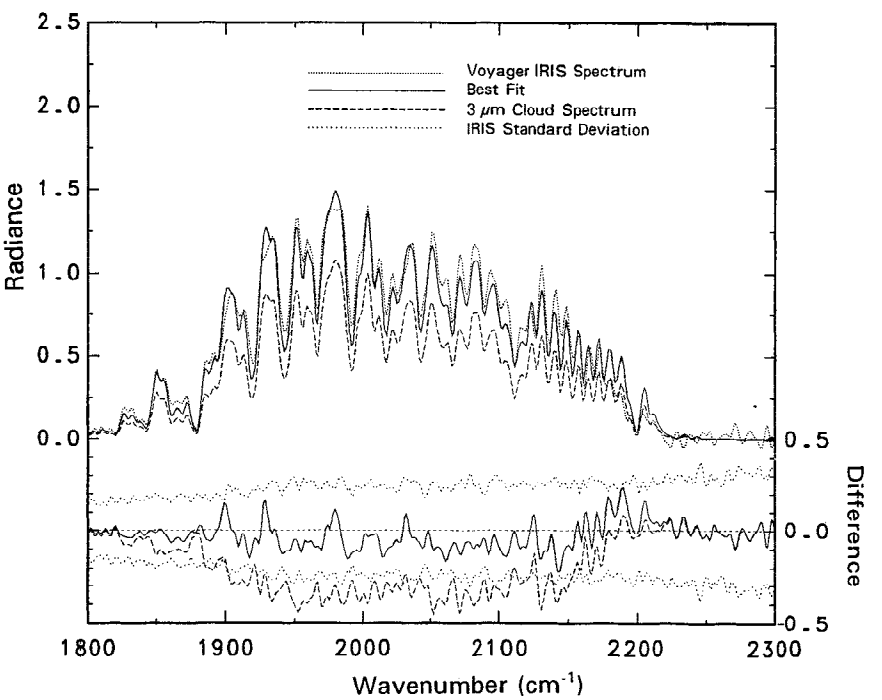


**Figure 16b.** Same as Figure 16a but for the 5-$\mu$m region.

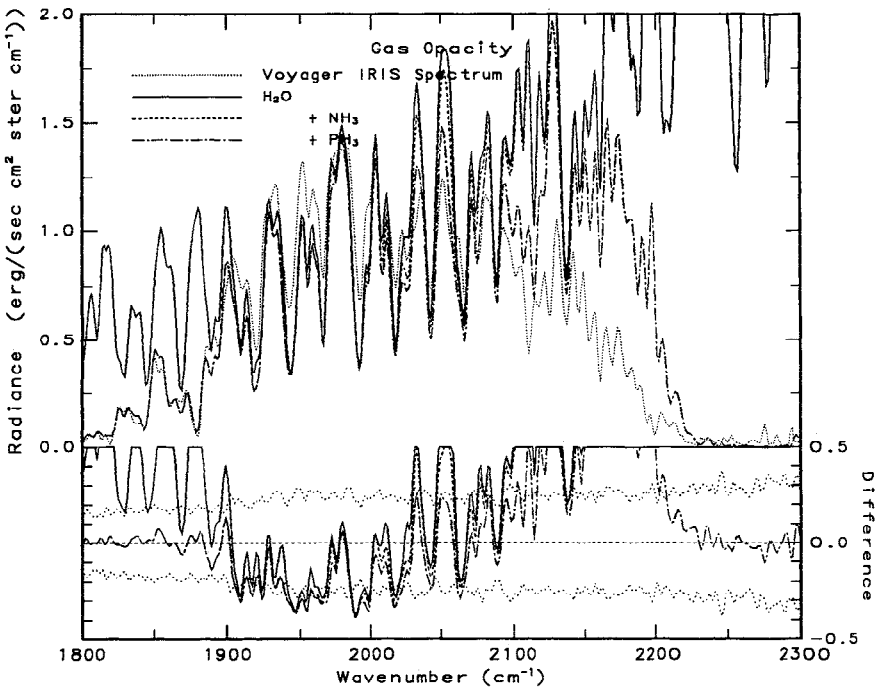


**Figure 17a.** Sensitivity of the 5-$\mu$m spectral region to the various sources of gaseous opacity. Synthetic spectra calculated with $H_2O$ opacity (solid line), $H_2O$ and $NH_3$ opacity (dashed line) and $H_2O$, $NH_3$, and $PH_3$ opacity (dash-dot line) are compared. The average IRIS NEB hot spot spectrum (dotted line) is also shown for comparison.

cloud opacity results in an acceptable fit to the 2150–2200 $cm^{-1}$ region. However, as also shown in Figure 18 (dash-dot line), while it is possible to fit the continuum level in the 2150–2200 $cm^{-1}$ region by increasing the optical depth of the $NH_4SH$ cloud, the fit at lower frequencies is no longer acceptable.

A more serious problem is that none of these spectra provide an acceptable fit to the 1900–2100 $cm^{-1}$ region of the

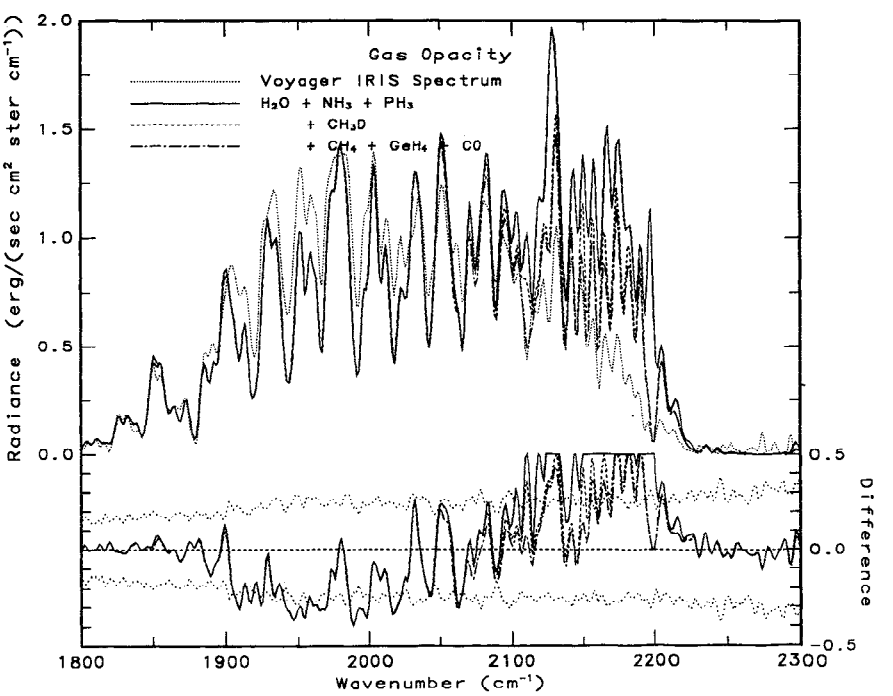


**Figure 17b.** Same as Figure 17a but synthetic spectra calculated with $H_2O$, $NH_3$, and $PH_3$ opacity (solid line) $H_2O$, $NH_3$, $PH_3$, and $CH_3D$ opacity (dashed line), and all sources of gaseous opacity in the 5-$\mu$m region (dash-dot line) are compared.

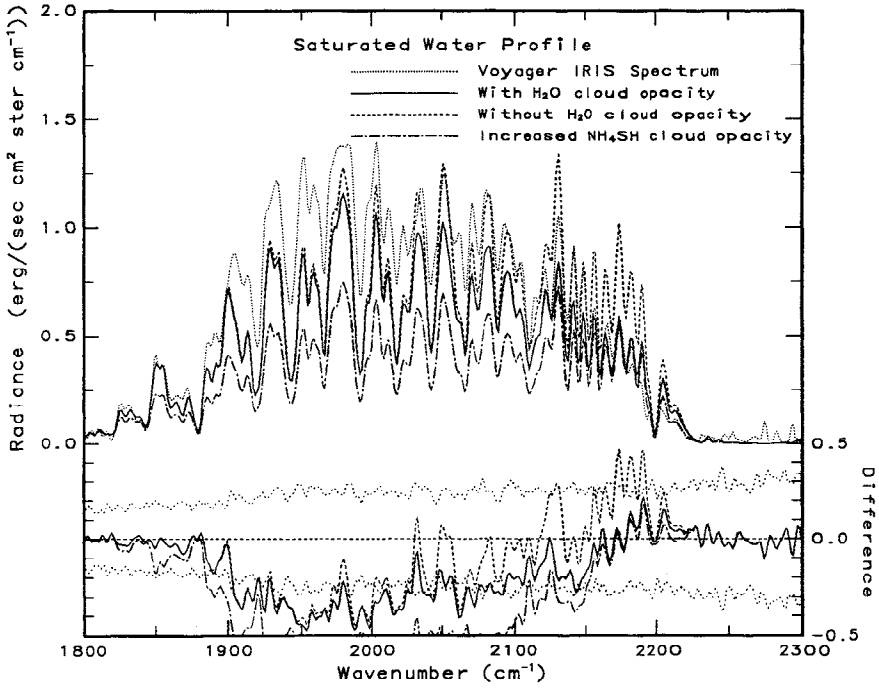


**Figure 18.** Comparison of synthetic spectra calculated with a saturated water profile and the inclusion of spectrally dependent water cloud extinction (solid line), without the inclusion of water cloud extinction (dashed line), and without the inclusion of water cloud extinction but with the optical depth of the $NH_4SH$ cloud increased to fit the continuum in the 2150–2200 $cm^{-1}$ region (dash-dot line). The average IRIS NEB hot spot spectrum (dotted line) is also shown. The well-mixed $H_2O$ mixing ratio is $2.76 \times 10^{-3}$ (2× solar).

spectrum. Here the continuum level is too low and the water absorption features are too strong. Clearly, a saturated water profile is unacceptable. Referring back to Figure 6, which shows the location of the peak emission level, we see that radiation in the 1900–2100 $cm^{-1}$ region of the spectrum originates at pressures between 2 and 4 bars. Hence it is necessary to reduce the relative humidity of water in the 2- to 4-bar region to fit the spectrum. (This is analogous to the situation for $NH_3$ in the far infrared, where a saturated $NH_3$ profile provides an unacceptable fit and we, as well as *Kunde et al.* [1982], have to conclude that the $NH_3$ vapor profile is subsaturated.)

Allowing the water vapor profile to saturate at cloud base (near 5 bars) and reducing the relative humidity of water from 100% (saturated) to 30% above the cloud (pressures less than 4 bars) result in a greatly improved fit to the spectrum, as shown in Figure 19 (solid line). That water cloud opacity is still required is illustrated by the comparison with the other synthetic spectra in Figure 19. If we remove the opacity provided by the water cloud (dashed line), we get an unacceptable fit to continuum portions of the spectrum from 1950 to 2200 $cm^{-1}$. If we try to reduce the continuum level, in the absence of water cloud opacity, by increasing the optical depth of the $NH_4SH$ cloud from 0.02 (our best fit value, dashed line) until the continuum level in the 2100–2200 $cm^{-1}$ region is fit, $\tau = 1.0$ (dash-dot line), the resultant spectrum provides a poor fit to the observations from 1900 to 2100 $cm^{-1}$.

As an aside, we note that the $NH_4SH$ cloud alone cannot provide the requisite cloud opacity. This is illustrated in Figure 20, which compares synthetic spectra calculated in the absence of water cloud opacity with $NH_4SH$ cloud optical depths of 0.2 (solid line), 0.5 (dashed line), and 1.0 (dash-dot line). Too little $NH_4SH$ opacity results in an unacceptable fit to the continuum in the 2150–2200 $cm^{-1}$ region, but when the optical depth of the $NH_4SH$ cloud is increased until the synthetic and observed spectra agree in the 2150–2200 $cm^{-1}$ region, then the 1900–2100 $cm^{-1}$ region of the spectrum is poorly fit. However, the artificial case of a perfect absorber (i.e., blackbody) with a single optical depth at all frequencies (i.e., spectrally gray), such as that used by *Bjoraker et al.* [1986], can provide a reasonable fit to the data due to the enhanced self-emission from the black cloud (i.e., this cloud is a perfect emitter), which as shown in Figure 17 of *Carlson et al.* [1992a] introduces a strong spectral slope in the 1800–1950 and 2190–2250 $cm^{-1}$ regions of the spectrum. This highlights the importance of a self-consistent analysis. When spectrally dependent cloud extinction is included (i.e., when the optical properties of $NH_4SH$ are used), the *Bjoraker et al.* [1986] solution of an optically thick cloud in the 2-bar region is no longer viable.

Thus the best argument in favor of the presence of the water cloud is the need for additional opacity in the 2150–2200 $cm^{-1}$ region of the spectrum, which based on the location of the peak emission level shown in Figure 6, is sensitive to pressures greater than 4 bars. From this, we conclude that a cloud must be present at pressures near 5 bars, which based on the coincidence between the location of this cloud and the saturation level for water, leads us to infer that this cloud is most likely composed of water. Moreover, the presence of a water cloud near 5 bars (i.e., supersolar abundance of water and a saturated profile near 5 bars) reconciles the low (subsaturated) abundances of water and hence oxygen in 2- to 4-bar region of the atmosphere, which is above the water cloud and therefore not representative of the deep, well-mixed abundance of water previ-

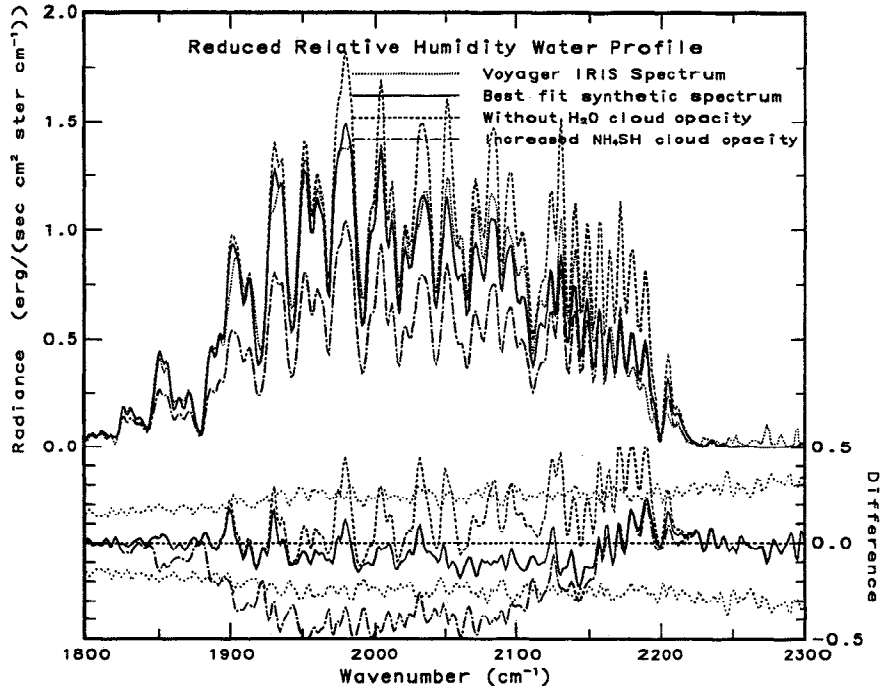


**Figure 19.** Same as Figure 18 except that the $NH_4SH$ cloud opacity is constrained by the fit in the 2100–2200 $cm^{-1}$ region of the spectrum.

ously inferred by *Kunde et al.* [1982] and *Bjoraker et al.* [1986] with the observed enhancements, with respect to solar abundances, of carbon and nitrogen and provides a physical mechanism capable of producing the height-dependent profiles inferred by both Kunde et al. and Bjoraker et al. Thus we conclude that the well-mixed abundance of water is at least 1.5 times solar, with 2 times solar providing our preferred fit [*Carlson et al.*, 1992a]. Our preference for a 2× solar enhancement is based on the vertical correlation between the clouds and the roughly 2× solar enhancement of C/H and N/H in the Jovian atmosphere.

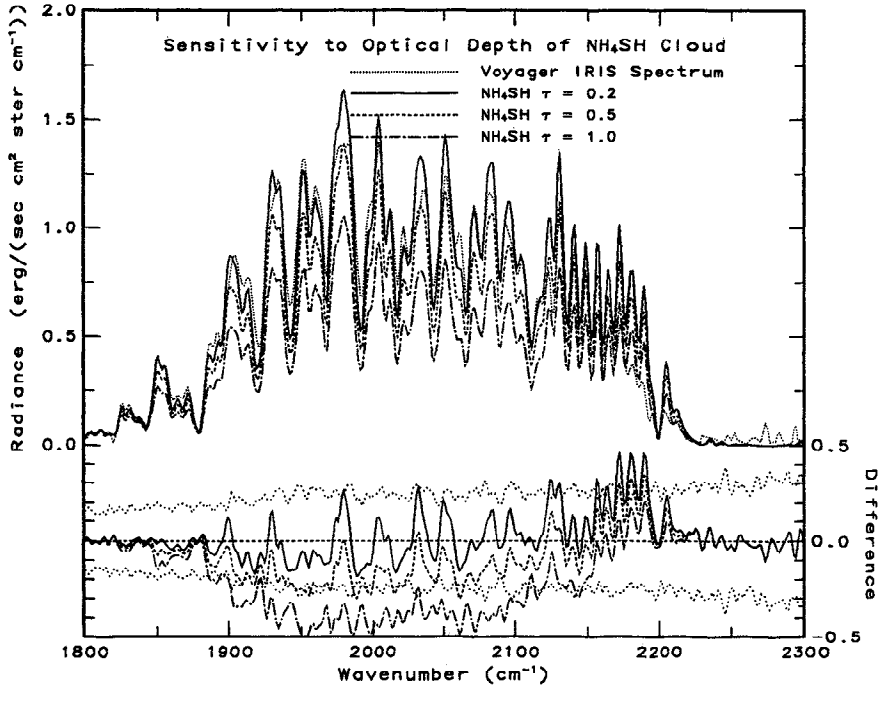


**Figure 20.** Illustration of the spectral sensitivity to the $NH_4SH$ cloud. Comparison of synthetic spectra calculated with $NH_4SH$ cloud optical depths of 0.2 (solid line), 0.5 (dashed line), and 1.0 (dash-dot line) with the average IRIS NEB hot spot spectrum (dotted line).

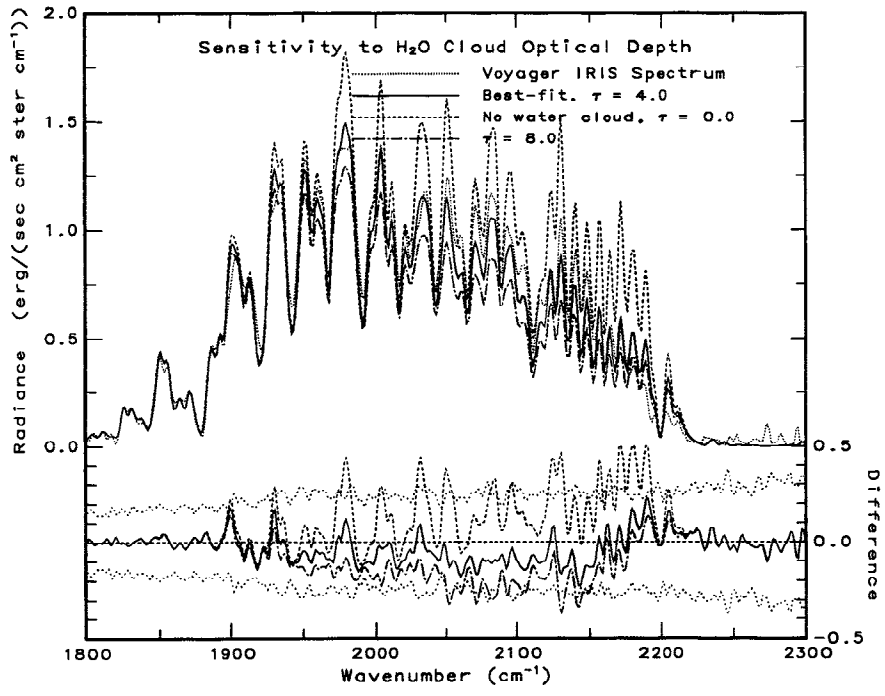


**Figure 21.** Illustration of the spectral sensitivity to the optical depth of the $H_2O$ cloud. Comparison of synthetic spectra calculated with water cloud optical depths of 4.0 (solid line), 0 (no water cloud opacity, dashed line), and 8.0 (dash-dot line) with the average IRIS NEB hot spot spectrum (dotted line).

The IRIS measurements require cloud opacity in the 5-bar region but cannot constrain the cloud base locations. Since water is saturated near 5 bars, we can only determine a lower limit on its abundance, and consequently, we cannot uniquely constrain the optical depth of the water cloud or its vertical distribution. However, once we have assumed an abundance (i.e., $2.76 \times 10^{-3}$), which determines cloud base, the IRIS spectra are sensitive to variations of the optical depth of the water cloud and the vertical distribution of water cloud opacity.

Figure 21 shows the spectral sensitivity to the optical depth of the water cloud: values as large as $\tau = 8$ are precluded. Figure 22 shows the spectral sensitivity to the vertical distribution of water cloud opacity: decreasing the vertical extent of the cloud by decreasing $H_p/H_g$ from 0.15 to 0.05 (dashed line) results in a poor fit to the IRIS observations because cloud opacity is confined to pressures greater than 4.5 bars. Similarly, increasing the vertical extent of the cloud by increasing $H_p/H_g$ from 0.15 to 0.25 (dash-dot line) results in a poor fit because cloud opacity is distributed too high in the atmosphere.

Thus, while our solution in terms of the well-mixed water abundance, the optical depth of the water cloud, and the vertical distribution of water cloud opacity is not unique, the amount of cloud opacity required at pressures less than 5 bars is uniquely constrained. As shown by *Carlson et al.* [1992a], a 10× solar abundance of water also provides an acceptable fit to the IRIS measurements. However, in that case, the relative humidity profile of water is saturated at pressures greater than 4.6 bars (above which the relative humidity profile follows that retrieved for the case of a 2× solar abundance of water) and the vertical extent and the optical depth of the water cloud have to be increased to $H_p/H_g = 0.25$ and $\tau = 10$ to get the requisite amount of cloud opacity in the 4- to 5-bar region of the atmosphere from the cloud base at 7 bars. The key is that the amount of water cloud opacity above the 5-bar level is unchanged between the best fit 2× and 10× solar solutions.

Finally, with the cloud properties constrained, we reexamine the gas abundance profiles. In particular, the IRIS measurements in the 1800–1900 $cm^{-1}$ region provide constraints on the abundance of $NH_3$ at pressures less than 3 bars (cf. Figure 6), i.e., well above the water cloud but below the $NH_3$ and $NH_4SH$ clouds. If aqueous chemical reactions occur in the Jovian atmosphere [*Carlson et al.*, 1987], this "deep" abundance represents only a lower limit. Figure 23 shows a comparison of synthetic spectra calculated with a constant mixing ratio below the $NH_3$ condensation level set to $8.9 \times 10^{-5}$ (solid), $1.78 \times 10^{-4}$ (solar, dashed line), and $4.45 \times 10^{-4}$ (dash-dot line). From this comparison, we see that none of these spectra fit the average IRIS NEB hot spot spectrum (dotted line) well. A solar abundance provides the best fit from 1827 to 1850 and 1860 to 1880 $cm^{-1}$, however, it does not provide an acceptable fit from 1850 to 1860 $cm^{-1}$, where an enhanced abundance of $NH_3$ provides the only acceptable fit. In interpreting this result, it is important to keep in mind the spectral dependence of the peak emission level shown previously in Figure 6b. As can be seen from the location of the peak emission level, radiation in the spectral intervals from 1827 to 1850 and 1860 to 1880 $cm^{-1}$ originates at pressures less than 2 bars, while radiation in the spectral interval from 1850 to 1860 $cm^{-1}$ originates at pressures greater than 2.2 bars. This suggests that the abundance of $NH_3$ decreases in the 2-bar region, consistent with the formation of an $NH_3$-containing condensate such as $NH_4SH$. The relative location of the peak emission level to the $NH_4SH$ cloud base suggests that the 1850–1860 $cm^{-1}$ interval is sensitive to the "well-mixed" (i.e., below the

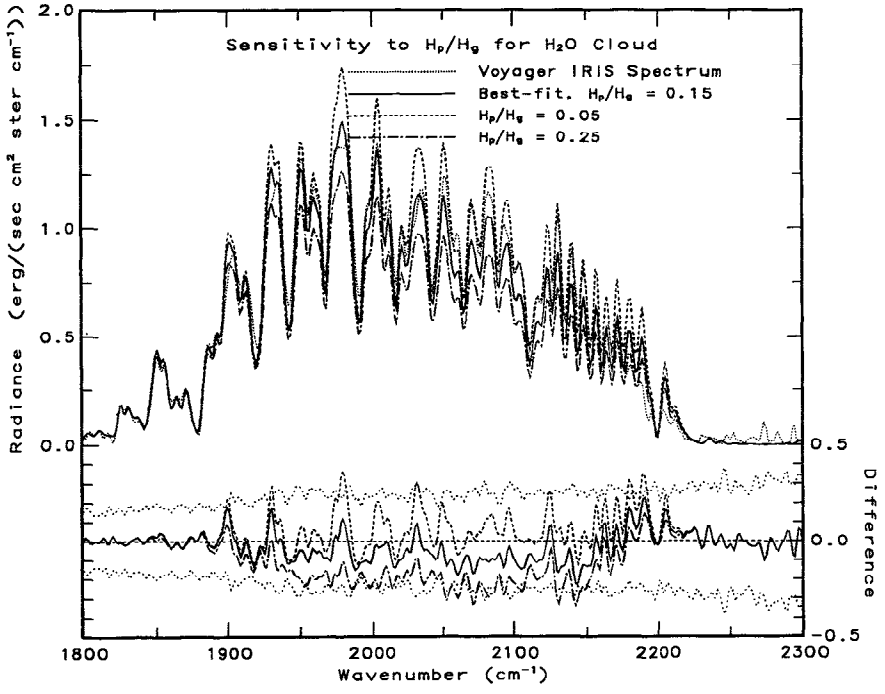


**Figure 22.** Illustration of the spectral sensitivity to the vertical distribution of water cloud opacity. Comparison of synthetic spectra calculated with $H_p/H_g$ = 0.15 (solid line), 0.05 (dashed line), and 0.25 (dash-dot line) with the average IRIS NEB hot spot spectrum (dotted line).

$NH_4SH$ cloud) $NH_3$ abundance, while the 1827–1850 and 1860–1880 $cm^{-1}$ spectral intervals are sensitive to the $NH_3$ abundance within the $NH_4SH$ cloud. Moreover, as shown previously in Figure 10, height-independent mixing ratios as large as $8.9 \times 10^{-5}$ at the 1-bar level provide a poor fit to the far-infrared spectrum, suggesting that the $NH_3$ mixing ratio continues to decrease above the 2-bar level, providing additional support for an $NH_3$-containing condensate near 2 bars. Based on the results shown in Figures 10 and 23, we conclude that the $NH_3$ mixing ratio must decrease between 3 bars and 1 bar, consistent with the formation of an additional $NH_3$-containing condensate, presumably $NH_4SH$. Thus the height dependence of the $NH_3$ profile provides additional support for the presence of an $NH_4SH$ cloud.

## 4. Results

The observed 45- and 5-$\mu$m brightness temperature relationship, previously shown in Figure 5, suggests that the extremes of cloud structure are likely to correspond to the end-members of this brightness temperature distribution (i.e., hot at both 45 and 5 $\mu$m; warm at 45 $\mu$m and cold at 5 $\mu$m; and cold at both 45 and 5 $\mu$m). In this section we use an anisotropic multiple scattering radiative transfer model [*Carlson et al.*, 1993] to analyze the spectral ensembles corresponding to these end-members (Table 2). Since in this paper, we are primarily interested in understanding the differences between belts and zones in terms of their cloud cover, we begin with an analysis of the IRIS data in the upper right-hand corner of Figure 5 because they correspond to the most transparent regions on Jupiter and therefore provide us with the best opportunity to study the deep cloud structure. Although the discussion highlights particular spectral or atmospheric features, the analysis of each spectral ensemble provides a fit to the IRIS spectrum at all frequencies to within the uncertainties defined by the variations among the spectra in the ensemble.

### 4.1. NEB Hot Spots

Our initial spectral ensemble corresponds to NEB hot spots, spectra with 45-$\mu$m brightness temperatures in excess of 149 K and 5-$\mu$m brightness temperatures in excess of 250 K. We begin with an analysis of the far-infrared region of the spectrum. Since we have used the hot spot spectral ensemble to illustrate the spectral sensitivity to the model parameters in the previous section, we will refer back to that discussion. Moreover, a more detailed description of our analysis of the NEB hot spot ensemble can be found in the work by *Carlson et al.* [1993]. As previously shown in Figure 12, $NH_3$ cloud opacity is required to fit the continuum in the 45-$\mu$m (226 ± 4 $cm^{-1}$) region of the spectrum. From the average NEB hot spot spectrum, we retrieve an $NH_3$ cloud optical depth of 0.27 ± 0.03. Our best fit suggests that the $NH_3$ cloud contains a mixture of large (effective radius of 100 $\mu$m, $\tau$ = 0.19) and small (effective radius of 3 $\mu$m, $\tau$ = 0.08) particles; however, the small-particle mode is not strictly required to fit the average spectrum, but does decrease the difference between the synthetic and observed spectra.

Since $NH_3$ cloud opacity affects the outgoing radiation in the wings of the S(0) hydrogen line, a height-independent para hydrogen profile, as previously shown in Figure 13, no longer provides an acceptable fit to these IRIS measurements. We model the height dependence of the para hydrogen profile by specifying the inflection points $P_L$ and $P_U$, which define the location of the para hydrogen gradient. The gradient is located between pressures $P_L$ and $P_U$, where $P_L$

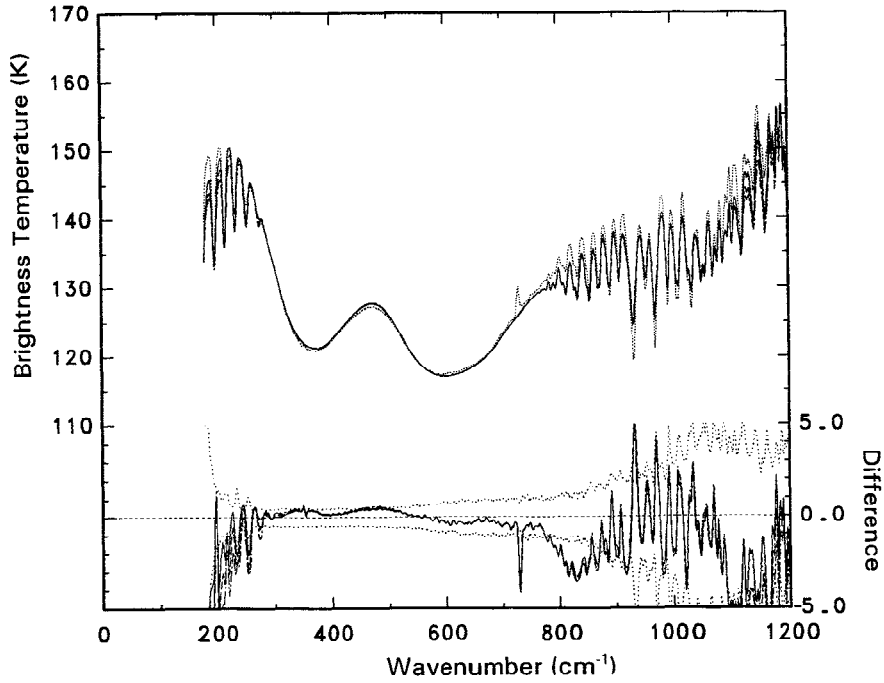


**Figure 23a.** Sensitivity of the spectra to the "well-mixed" abundance of $NH_3$. Comparison of synthetic spectra calculated with a well-mixed abundance of $8.9 \times 10^{-5}$ (solid line), $1.78 \times 10^{-4}$ (solar, dashed line), and $4.45 \times 10^{-4}$ (dash-dot line) with the average IRIS NEB hot spot spectrum (dotted line) in the far-infrared spectral region. The $NH_3$ abundance is constant with height below the $NH_3$ condensation level.

is the lower inflection point and $P_U$ is the upper inflection point. Below pressure $P_L$ the para fraction is constant at the deep atmosphere "normal" value, between $P_L$ and $P_U$ the para fraction linearly increases from the normal value at and below $P_L$ to the more equilibrated value found at and above $P_U$. As shown in Figure 7 of *Carlson et al.* [1992b], the inflection points are well constrained by the IRIS measurements. Our best fit para fraction profile is specified by $P_L = 0.5 \pm 0.1$ bar, $P_U = 0.2 \pm 0.1$ bar, $f_p = 0.25$ at pressures greater than 0.5 bars, and $f_p = 0.32 \pm 0.01$ at pressures less than 0.2 bars.

Figure 24 illustrates the spectral sensitivity to the para

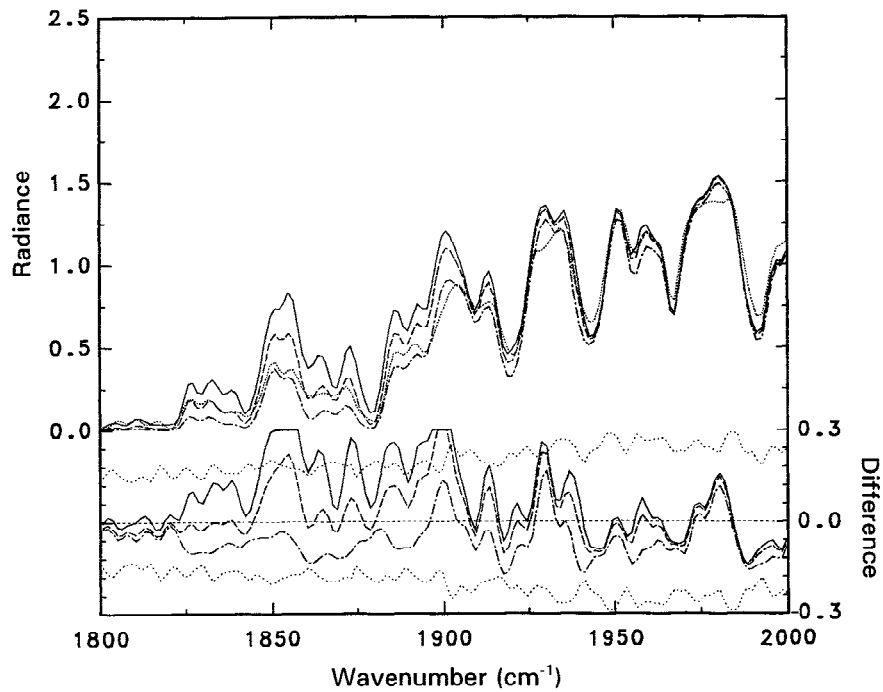


**Figure 23b.** Same as Figure 23a but for the 1800–2000 cm$^{-1}$ spectral region.

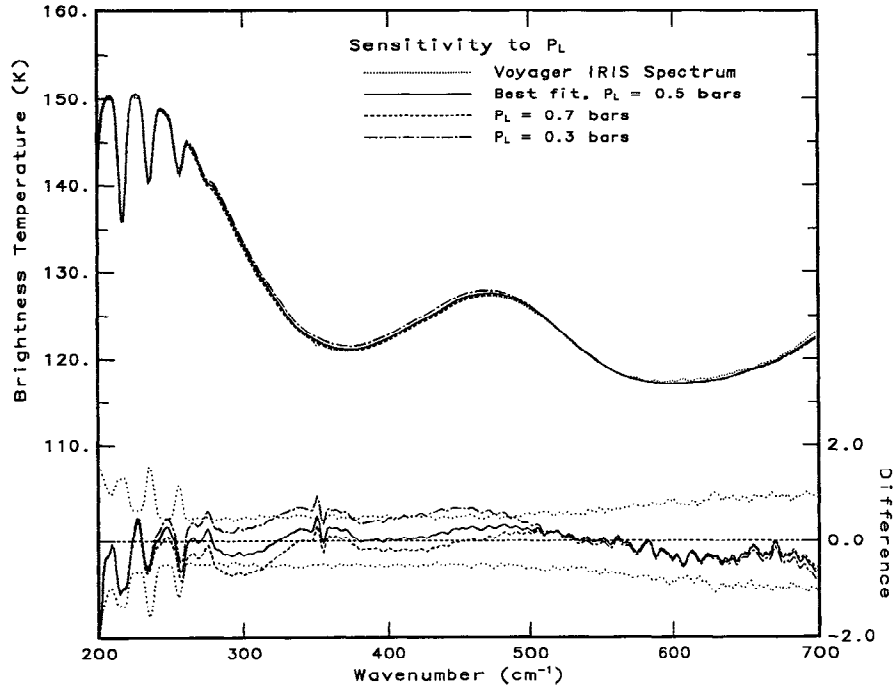


**Figure 24a.** Illustration of the spectral sensitivity to the height-dependent para hydrogen profile. The sensitivity to the lower inflection point $P_L$ is shown as well as the comparison of the synthetic spectra calculated with $P_L$ = 0.5 (solid line), 0.7 (dashed line), and 0.3 bar (dash-dot line). The average IRIS NEB spectrum (dotted line) is shown for comparison in Figures 24a–24d.

hydrogen profile and also shows that the 180–210 $cm^{-1}$ region of the spectrum is insensitive to the para hydrogen profile, which allows us to separate the effects of $NH_3$ cloud opacity and para hydrogen in the 200–300 $cm^{-1}$ region of the spectrum. The locations of the upper and lower inflection points are well constrained by the IRIS measurements. As shown in Figure 24a, the lower inflection point $P_L$ is constrained to be 0.5 ± 0.1 bar. Shifting the location of this inflection point to pressures as large as 0.7 bar (dashed line) increases absorption too much because of the increased para fraction in the 0.5-bar region, resulting in a poor fit to the IRIS measurements. Shifting the location of the $P_L$ to

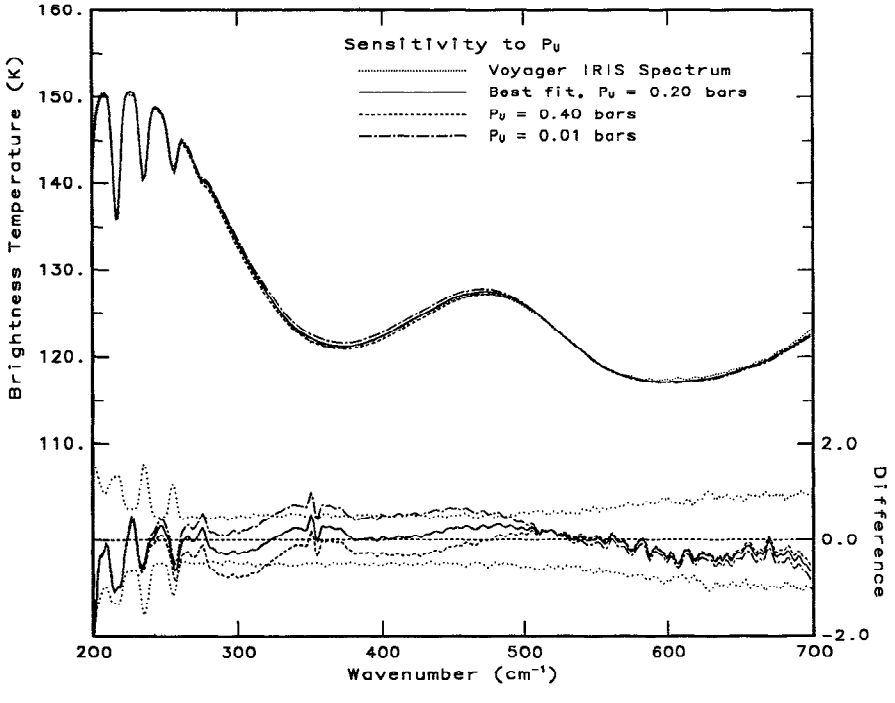


**Figure 24b.** The sensitivity to the upper inflection point $P_U$ and comparison of synthetic spectra calculated with $P_U$ = 0.2 (solid line), 0.4 (dashed line), and 0.01 bar (dash-dot line).

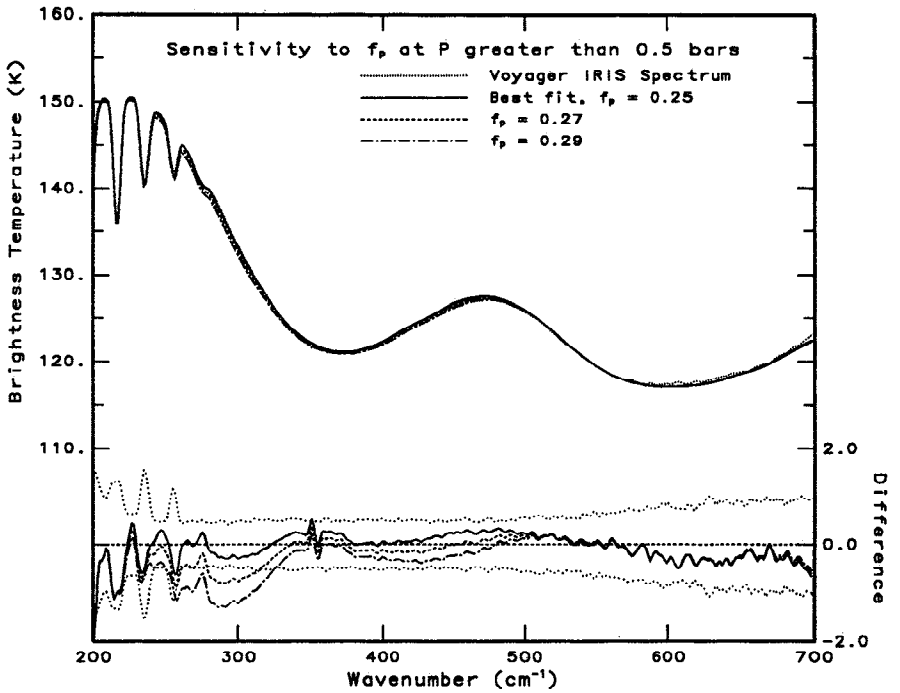


**Figure 24c.** The sensitivity to the value of $f_p$ at depth ($P > 0.5$ bar) and comparison of synthetic spectra calculated with $f_p = 0.25$ (solid line), 0.27 (dashed line), and 0.29 (dash-dot line).

pressures as low as 0.3 bar (dash-dot line) decreases the absorption too much by reducing the para fraction in the 0.5-bar region, also resulting in a poor fit to the IRIS measurements. The effect that shifting the location of the upper inflection point $P_U$ has on the spectrum is illustrated in Figure 24b. As shown, shifting the location of $P_U$ from 0.2 to 0.4 bar, increases the para fraction at pressures less than 0.5 bar, resulting in too much absorption and a poor fit to the IRIS measurements. Likewise, shifting $P_U$ to lower pressure (allowing the equilibration process to continue above the $NH_3$ cloud top) results in too little absorption and a poor fit to the IRIS measurements. Figure 24 shows that some trade-offs exist among the parameters specifying the para hydrogen profile. For example, shifting $P_U$ to higher pressure results in increased absorption, but this effect can be offset, to some degree, by decreasing $f_p$ at pressures less

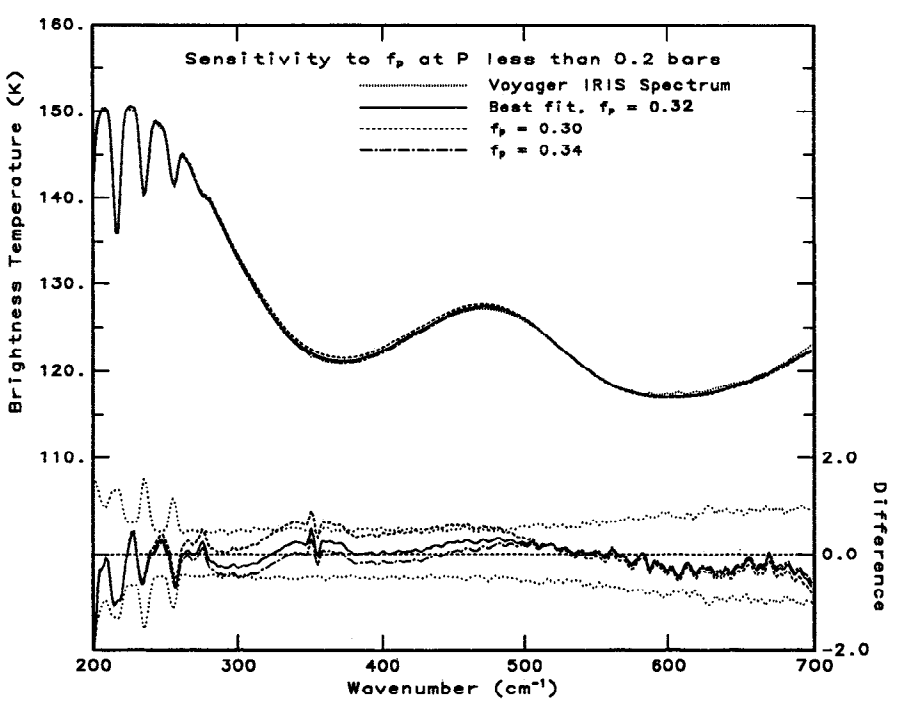


**Figure 24d.** The sensitivity to the value of $f_p$ aloft ($P < 0.2$ bar) and comparison of synthetic spectra calculated with $f_p = 0.32$ (solid line), 0.30 (dashed line), and 0.34 (dash-dot line).

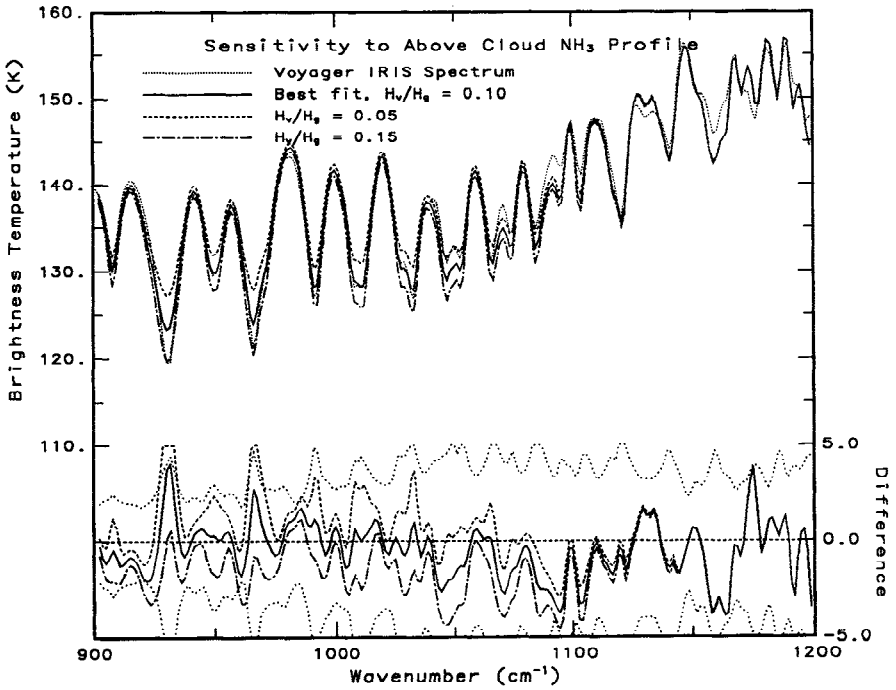


**Figure 25.** Illustration of the spectral sensitivity in the 900–1200 $cm^{-1}$ region to the height dependence of the $NH_3$ vapor profile above the $NH_3$ condensation level. Comparison is shown between synthetic spectra calculated with $H_v/H_g$ = 0.10 (solid line), 0.05 (dashed line), and 0.15 (dash-dot line) and the average IRIS NEB hot spot spectrum (dotted line).

than $P_U$. Thus the IRIS measurements are sensitive to the para hydrogen gradient, and location of the gradient.

The values of the para fraction at pressures greater than 0.5 bar and less than 0.2 bar are also well constrained by the IRIS measurements. As shown in Figure 24c, para fractions of 0.27 and 0.29 at pressures greater than 0.5 bar are clearly precluded; as shown in Figure 24d, para fractions of 0.3 and 0.34 clearly provide a poorer fit.

The far infrared observations are also sensitive to the vertical distribution of $NH_3$ gas within and above the $NH_3$ cloud. Consistent with the results of *Kunde et al.* [1982], we find that the $NH_3$ profile above 0.5 bar is significantly subsaturated. This is most likely a consequence of the combined effects of dynamics and photochemistry. We model this height dependence using a vapor-to-gas scale height ratio, which for the NEB hot spots is 0.10 ± 0.02. The sensitivity of the IRIS measurements to the $NH_3$ profile is illustrated in Figure 25. Our best fit spectrum has $H_v/H_g$ = 0.1 (solid line), which causes the $NH_3$ mixing ratio to decrease from $3 \times 10^{-5}$ at 0.5 bar to $1.7 \times 10^{-7}$ at 0.3 bar. Decreasing the value of $H_v/H_g$ to 0.05 (dashed line) results in a much sharper decrease in the $NH_3$ mixing ratio with height to give a mixing ratio of $6 \times 10^{-10}$ at 0.3 bar. In this case, there is not enough $NH_3$ opacity at pressures less than 0.5 bar. Increasing the value of $H_v/H_g$ to 0.15 (dash-dot line) results in a more gradual decrease in the $NH_3$ mixing ratio with height: the mixing ratio of $NH_3$ at 0.3 bar is $1 \times 10^{-6}$, which provides too much opacity at pressures less than 0.5 bar.

The 900–1200 $cm^{-1}$ spectrum is affected by the vertical distribution of $PH_3$ above the 1-bar level, where photochemical reactions destroy $PH_3$. We model this height dependence using a vapor-to-gas scale height ratio as for $NH_3$. Above 1 bar, the $PH_3$ abundance falls off following a vapor-to-gas scale height ratio of 0.3 ± 0.15. The sensitivity of the IRIS measurements to the height dependence of the $PH_3$ profile is illustrated in Figure 26. In our best fit spectrum (solid line), $H_v/H_g$ = 0.30, giving a mixing ratio of $PH_3$ of $3.4 \times 10^{-8}$ at 0.3 bar. Decreasing $H_v/H_g$ to 0.15 (dashed line) results in an unacceptable fit to the IRIS measurements, as a mixing ratio as small as $6 \times 10^{-10}$ at 0.3 bar provides too little absorption. Increasing $H_v/H_g$ to 0.45 (dash-dot line) also provides an unacceptable fit to the IRIS measurements, as a mixing ratio as large as $1 \times 10^{-7}$ at 0.3 bar provides too much opacity. Thus the IRIS measurements are sufficient to conclude that $PH_3$ has a height-dependent profile and provides some constraints on the mixing ratios in the upper troposphere. (The well-mixed abundance of $PH_3$ is constrained by the 5-$\mu$m spectrum.)

With the upper tropospheric properties constrained, we turn our attention to the 5-$\mu$m measurements. The mini-window near 2130 $cm^{-1}$ is one of the most transparent regions in the Jovian spectrum. As previously shown in Figures 18–20, to fit the observed spectrum, this region requires additional opacity near the 5-bar level for which the water cloud is the only plausible source. Our best fit spectrum is obtained with a 2× solar abundance of water ($2.76 \times 10^{-3}$), resulting in a cloud base at 4.9 bars. Larger abundances of water can also produce acceptable fits, provided that the vertical extent and optical depth of the water cloud are increased to maintain the required opacity near the 5-bar level. Thus we can only retrieve a lower limit to the actual abundance of water in the deeper parts of Jupiter.

As was shown in Figures 18 and 19, a saturated water profile above cloud base results in too much opacity in the 2- to 4-bar region of the atmosphere, to which the 1900–2100 $cm^{-1}$ spectral interval is sensitive. By decreasing the relative humidity of water in the 2- to 4-bar region of the atmosphere, we are able to fit the continuum in this region of the

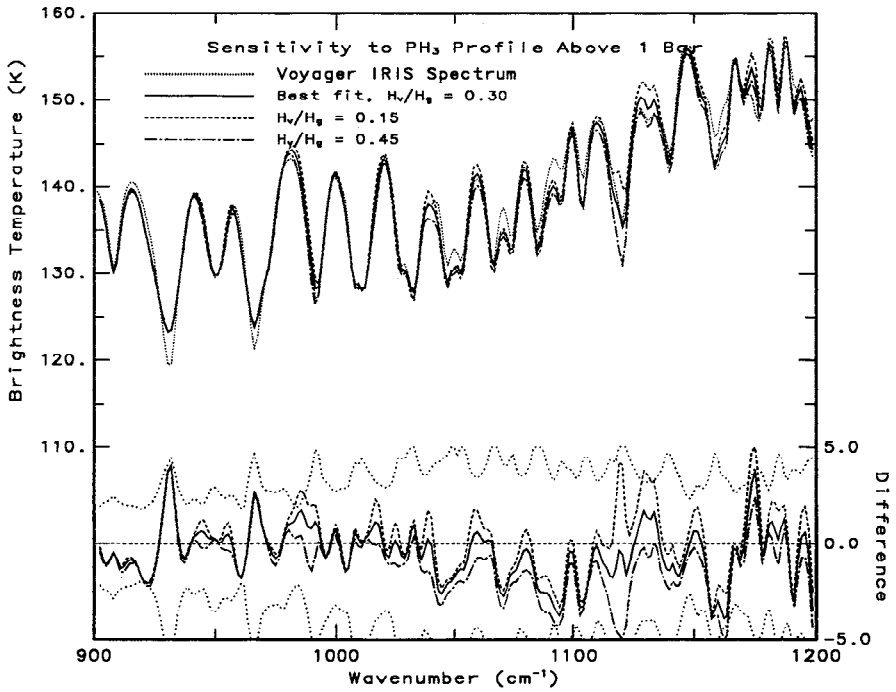


**Figure 26.** Illustration of the spectral sensitivity in the 900–1200 $cm^{-1}$ region to the height dependence of the $PH_3$ profile (well-mixed abundance of $PH_3$ is constrained by the 5-$\mu$m observations). Comparison is shown between synthetic spectra calculated with $H_v/H_g = 0.30$ (solid line), 0.15 (dashed line), and 0.45 (dash-dot line) and the average IRIS NEB hot spot spectrum (dotted line).

spectrum, as well as the depth of the absorption features. On the other hand, decreasing the well-mixed abundance of water (i.e., the *Bjoraker et al.* [1986] solution) shifts the location of the water cloud into the 2- to 4-bar region of the atmosphere and, as shown in *Carlson et al.* [1992a], results in an unacceptable fit to the IRIS measurements. In our best fit profile the relative humidity of water gradually decreases from 100% at cloud base (4.9 bars) to an above cloud minimum of 15% at 3 bars. Since the 5-$\mu$m measurements are relatively insensitive to the abundance of water in the 1-bar region, we find that the IRIS measurements can be fit with relative humidities in the range 15–100% near 1 bar. Thus it is possible that the relative humidity of water remains constant with height above 3 bars or that the relative humidity of water gradually increases to saturated values near 1 bar. Our best fit parameters to the NEB hot spot ensemble are summarized in Table 4.

**Table 4.** Summary of Our Best Fit Model Results

| Parameter | NEB Hot Spots | EqZ (Cold) | NTrZ (Cold) |
|---|---|---|---|
| Number of spectra | 52 | 32 | 86 |
| $\tilde{\mu}$ | 0.958 | 0.984 | 0.937 |
| $NH_3$ cloud | | | |
| $\tau^*$ | 0.27 ± 0.03 | 0.64 ± 0.05 | 0.97 ± 0.08 |
| $\tau_{\text{large particle}}$ | 0.19 | 0.58 | 0.92 |
| $H_p/H_g$ | 0.15 ± 0.10 | 0.20 ± 0.10 | 0.03 ± 0.10 |
| $P_{\text{bot}}$ | 0.52 | 0.52 | 0.50 |
| $NH_4SH$ cloud | | | |
| $\tau^*$ | $0.02^{+0.06}_{-0.02}$ | 5.3 ± 2.0 | 3.1 ± 1.5 |
| $H_p/H_g$ | 0.15 ± 0.10 | 0.35 ± 0.10 | 0.40 ± 0.10 |
| $P_{\text{bot}}$ | 1.9 | 1.9 | 1.8 |
| $H_2O$ cloud | | | |
| $\tau^*$ | 4.0 ± 1.0 | 15.0 | 15.0 |
| $H_p/H_g$ | 0.15 ± 0.10 | 0.20 ± 0.10 | 0.25 ± 0.10 |
| $P_{\text{bot}}$ | 4.9 | 4.9 | 5.0 |
| $NH_3$ at 1 bar | $(2.8 \pm 1.0) \times 10^{-5}$ | $(2.8 \pm 1.0) \times 10^{-5}$ | $(1.8 \pm 1.0) \times 10^{-5}$ |
| $NH_3$ $H_v/H_g$ | 0.10 ± 0.02 | 0.18 ± 0.02 | 0.15 ± 0.02 |
| $NH_3$ at 3 bars | $(4.5 \pm 0.2) \times 10^{-4}$ | $(4.2 \pm 0.4) \times 10^{-4}$ | $(4.4 \pm 0.4) \times 10^{-4}$ |
| $PH_3$ $H_v/H_g$ | 0.30 ± 0.15 | 0.45 ± 0.15 | 0.30 ± 0.15 |
| Para profile | | | |
| $P_U$ | 0.2 ± 0.1 | 0.2 ± 0.1 | 0.2 ± 0.1 |
| $P_L$ | 0.5 ± 0.1 | 0.4 ± 0.1 | 0.4 ± 0.1 |
| $f_p$ | 0.32 ± 0.01 | 0.33 ± 0.01 | 0.35 ± 0.03 |

*The reported optical depths are the reference ($\lambda = 0.5$ $\mu$m) optical depths.

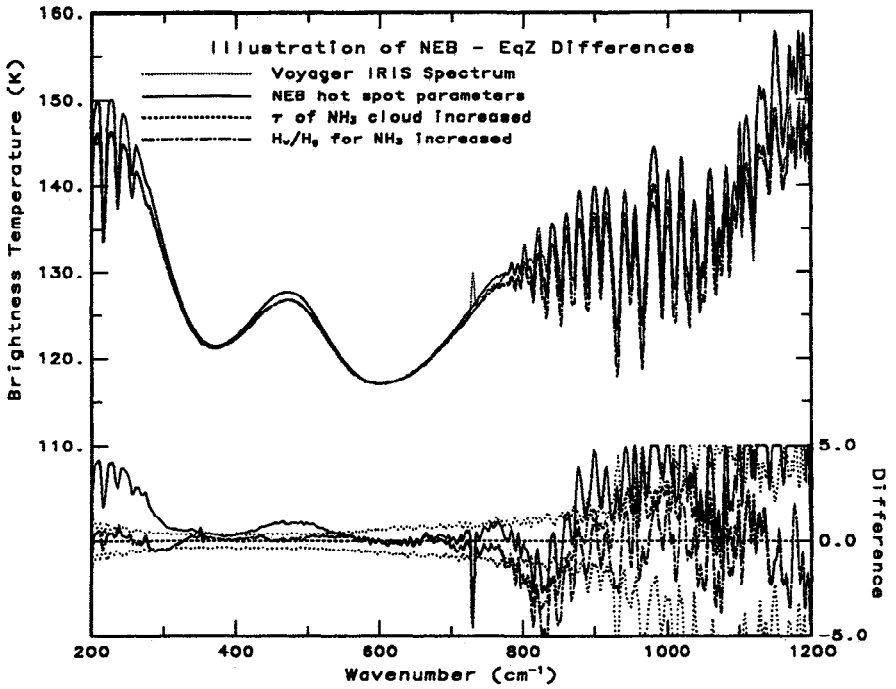


**Figure 27a.** Comparison of the average IRIS EqZ cold spectrum (dotted line) with synthetic spectra calculated using our best fit NEB model parameters (solid line), with the optical depth of the $NH_3$ cloud increased (dashed line), and with the vapor-to-gas scale height ratio for $NH_3$ increased (dash-dot line).

### 4.2. EqZ

The average 45- and 5-$\mu$m brightness temperatures associated with the EqZ spectra are generally a little colder and less variable than those in the NEB (Figures 7 and 8). Our extreme EqZ spectral ensemble is defined by average 45-$\mu$m brightness temperatures between 144 and 149 K and average 5-$\mu$m brightness temperatures between 180 and 205 K. This ensemble contains 32 IRIS spectra. As shown in Figure 27a, our NEB hot spot model parameters (solid line) provide a reasonable starting point for our analysis of the average IRIS

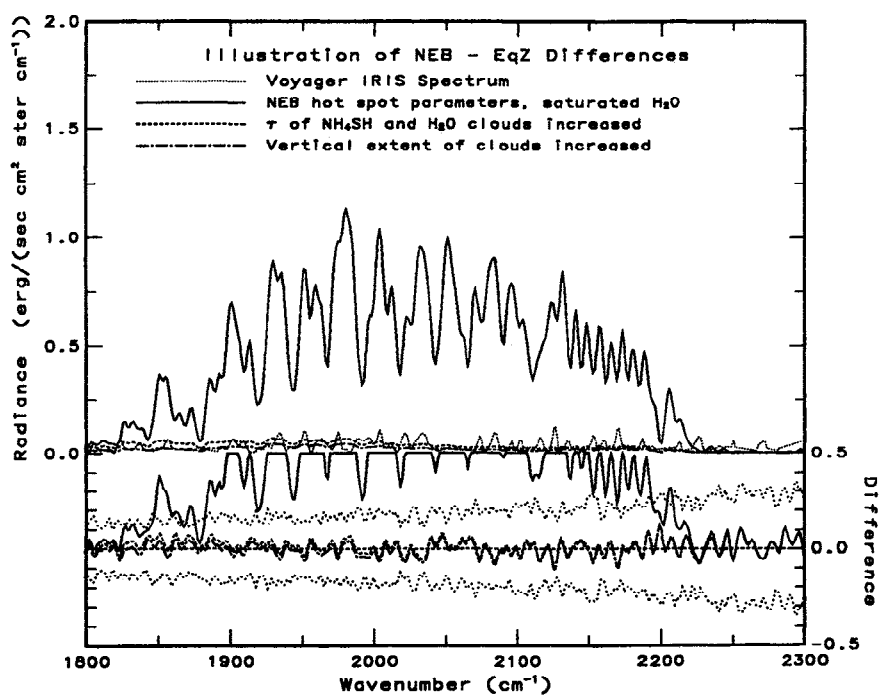


**Figure 27b.** Comparison of the average IRIS EqZ cold spectrum (dotted line) with synthetic spectra calculated with our best fit NEB cloud parameters but with a saturated water profile (solid line), with the optical depths of the $NH_4SH$ and $H_2O$ clouds increased (dashed line), and with the vertical extent of the $NH_4SH$ and $H_2O$ clouds increased (dash-dot line).

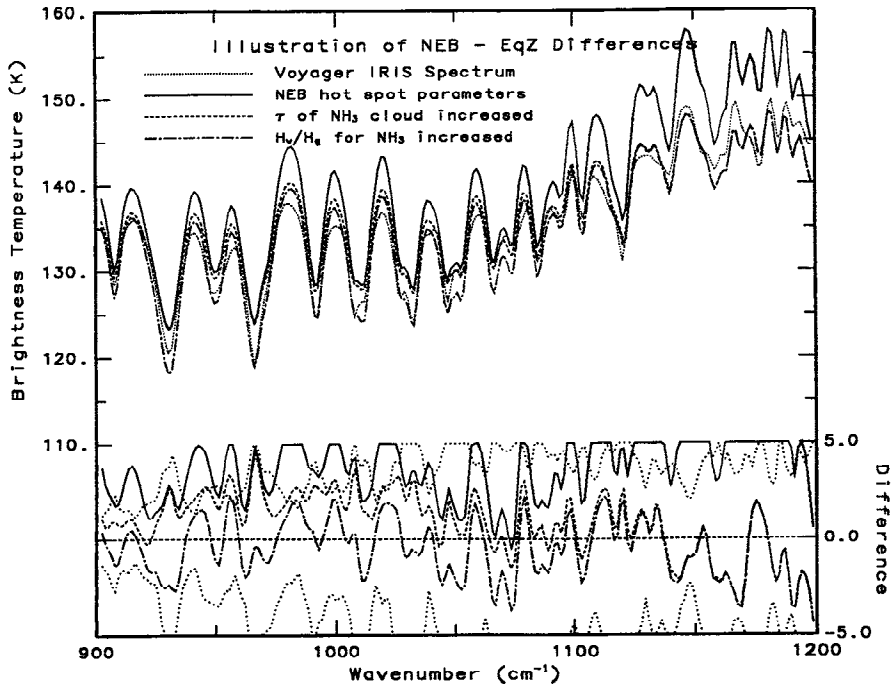


**Figure 28a.** Detailed comparison in the 900–1200 $cm^{-1}$ region between the synthetic and observed spectra shown in Figure 27. Comparison is shown between the synthetic spectra calculated with our best fit NEB hot spot parameters (solid line), with increased $NH_3$ cloud opacity (dashed line), and with an increased $NH_3$ vapor-to-gas scale height ratio (dash-dot line) and the average IRIS cold EqZ spectrum.

cold EqZ spectrum (dotted line) in the far infrared, but even with a saturated water profile, the best fit NEB parameters produce a 5-$\mu$m spectrum completely unlike the observed 5-$\mu$m spectrum (Figure 27b).

Since the continuum in the 200–300 $cm^{-1}$ region is particularly sensitive to the optical depth of the $NH_3$ cloud, the poor fit in this region is an indication that the optical depth of the $NH_3$ cloud has to be increased. As shown in Figure 27a, increasing the optical depth of the $NH_3$ cloud from 0.27 to 0.64 (dashed line) greatly improves the agreement between the synthetic and observed spectra in this spectral interval.

Similarly, the optical depths of the $NH_4SH$ and $H_2O$ clouds must be increased to fit the observations in the 5-$\mu$m region. Increasing the optical depth of the $NH_4SH$ cloud from 0.02 to 5.3 and increasing the optical depth of the $H_2O$ cloud from 4.0 to 15.0 (dashed line) improves the agreement between the synthetic and observed spectra in the 5-$\mu$m region (Figure 27b). Although the 5-$\mu$m spectral radiances appear close to zero in Figure 27b, the observed radiance is 0.053 erg $s^{-1}$ $cm^{-2}$ $sr^{-1}/cm^{-1}$ at 2000 $cm^{-1}$ compared with an instrumental noise level of 0.01 erg $s^{-1}$ $cm^{-2}$ $sr^{-1}/cm^{-1}$. Moreover, although we are using the standard deviation of the individual IRIS spectra to judge the goodness of our model fits, the high wavelength-to-wavelength precision of the IRIS measurements allows us to use the information contained in the shape of the spectrum and spectral slopes to retrieve the cloud properties. As shown in Figure 27b, the fit to the slope of the spectrum in the 1800–1950 $cm^{-1}$ spectral interval can be improved slightly by increasing the vertical extent of the $NH_4SH$ cloud. Increasing $H_p/H_g$ from 0.15 (dashed line) to 0.35 (dash-dot line) improves the agreement between the synthetic and observed spectra in the 1800–1950 $cm^{-1}$ interval.

Increasing the vertical extent of the $NH_4SH$ cloud also has an effect on the far-infrared spectral region. While the bulk of the $NH_4SH$ cloud opacity is distributed between 1.0 and 1.9 bars, some $NH_4SH$ cloud opacity now extends to 0.2 bar; thus $NH_4SH$ cloud opacity is mixed throughout the $NH_3$ cloud region. The impact of this $NH_4SH$ cloud opacity on the far-infrared spectrum is nonnegligible. Returning our focus to the far-infrared portion of the spectrum, the dashed and dash-dot lines in Figure 27a were calculated including the opacity provided by the $NH_4SH$ cloud with $\tau = 5.3$ distributed according to $H_p/H_g = 0.35$. If we look at the details of the fit in the 900–1200 $cm^{-1}$ region, shown in Figure 28a, we see that the increased optical depth of the $NH_3$ cloud (dashed line) generally improves the fit in the continuum regions but the depths of the $NH_3$ absorption features are still poorly fit, suggesting that there is more $NH_3$ in the upper troposphere of the cold EqZ regions than in NEB hot spots.

Increasing the amount of $NH_3$ in the upper troposphere by increasing the vapor-to-gas scale height ratio from 0.1 to 0.18 (dash-dot line; solid line in Figure 28b) results in an improved fit to the depth of the $NH_3$ absorption features. However, some regions, e.g., 980 $cm^{-1}$, remain poorly fit. This region of the spectrum is also sensitive to the vertical distribution of $PH_3$ above the 1-bar level. Increasing the vapor-to-gas scale height ratio governing the $PH_3$ profile from 0.3 to 0.45 (dashed line in Figure 28b) results in an improved fit to this spectral interval. The effect that $NH_4SH$ cloud opacity has on the far infrared can be seen in the comparison of the synthetic spectra shown by the dashed and dash-dot lines in Figure 28b. The only difference is that the vertical distribution of $NH_4SH$ cloud is specified by $H_p/H_g = 0.35$ in the spectrum shown by the dashed line and 0.15 in the spectrum shown by the dash-dot line. Clearly,

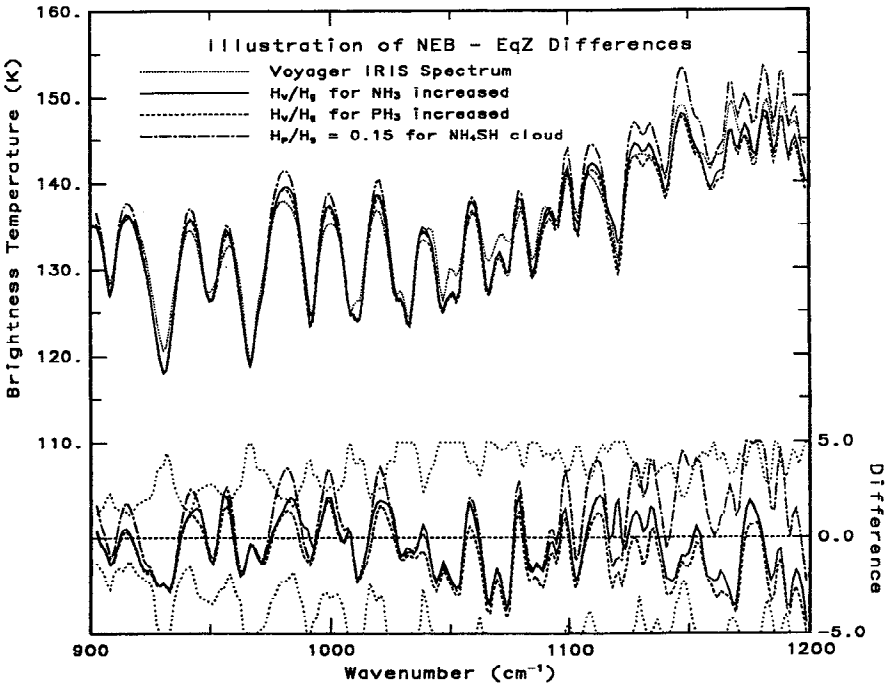


**Figure 28b.** Comparison between synthetic spectra calculated with $H_v/H_g = 0.18$ for $NH_3$ (solid line), with the vapor-to-gas scale height ratio for $PH_3$ increased (dashed line), and with the particle-to-gas scale height ratio of the $NH_4SH$ set to 0.15 (dash-dot line) and the average IRIS cold EqZ spectrum (dotted line). The difference between the spectra shown by the dashed and dash-dot lines illustrates the effect of $NH_4SH$ cloud opacity on the far-infrared spectrum.

$NH_4SH$ cloud opacity affects the spectrum in the 1100–1200 $cm^{-1}$ region.

Likewise, it is not possible to simultaneously fit the 200–300 and 1100–1200 $cm^{-1}$ regions simply by increasing the optical depth of the $NH_3$ cloud or the $NH_4SH$ cloud, which in our model provides a negligible contribution in the 200–300 $cm^{-1}$ region because the effective radii of the cloud particles are small (3 $\mu$m). The additional opacity that is required in the 1100–1200 $cm^{-1}$ region can only be supplied by the $NH_4SH$ cloud, since other gaseous absorbers, such as $CH_3D$, also affect some other spectral region, causing a poor fit. Moreover, it is not reasonable to consider spatial variations in the abundance of well-mixed constituents. This need for additional opacity in the 1100–1200 $cm^{-1}$ interval, coupled with the need to increase the vertical extent of the $NH_4SH$ cloud in order to improve the agreement between the synthetic and observed spectra in the 1800–1950 $cm^{-1}$ region, strongly argues that in these cold EqZ regions, $NH_4SH$ cloud opacity extends well above the 1-bar level.

While these parameters provide a good fit to most of the spectrum, the region near 300 $cm^{-1}$ is still poorly fit, as shown in Figure 29. Since this region of the spectrum is also sensitive to the para hydrogen gradient, increasing the para fraction above the 0.2-bar level from 0.32 to 0.33 and shifting $P_L$ from 0.5 to 0.4 bar, improves the agreement between the synthetic and observed spectra, as shown by the solid line. Our best fit parameters for this cold EqZ ensemble are summarized in Table 4.

### 4.3. NTrZ

The colder 45-$\mu$m brightness temperatures observed in the NTrZ suggest that the $NH_3$ cloud provides even more opacity in this region than in the EqZ. Moreover, the NTrZ has the most homogeneous distribution of 45- and 5-$\mu$m brightness temperatures, suggesting a fairly uniform cloud structure. Our NTrZ ensemble is defined by 45-$\mu$m brightness temperatures between 140 and 144 K and 5-$\mu$m brightness temperatures between 180 and 205 K (Table 2). Thus our NTrZ ensemble has a colder 45-$\mu$m brightness temperature and the same 5-$\mu$m brightness temperature selection criterion as our cold EqZ ensemble. This ensemble contains 86 individual IRIS spectra.

In agreement with the results of previous investigations, e.g., *Hanel et al.* [1979], we find that the NTrZ is physically colder than other regions; here the 1-bar temperature is 1.3°C colder than that in NEB hot spots. Figure 30a shows the fit to the NTrZ spectrum calculated with the optical depth of the $NH_3$ cloud increased to 0.97, roughly 1.5 times that found in the EqZ. As can be seen, an optical depth of 0.97 with $H_p/H_g = 0.15$ (solid line) provides an acceptable fit to the 900–1200 $cm^{-1}$ region but provides too much opacity in the 200–300 $cm^{-1}$ region. Reducing the vertical extent of the cloud, by decreasing $H_p/H_g$ to 0.03 (dashed line) results in an improved fit to the 200–300 $cm^{-1}$ region. By slightly increasing the complexity of the opacity distribution by concentrating the bulk of the cloud opacity near cloud base ($\tau = 0.85$) with a particle-to-gas scale height ratio of 0.03 and distributing a small amount of opacity ($\tau = 0.12$) according to $H_p/H_g = 0.2$ (dash-dot line) the difference between the synthetic and observed spectra is minimized. However, as can be seen from the difference plot, this is not strictly required by these IRIS measurements.

The effect that cloud opacity has on the 5-$\mu$m region of the spectrum is shown in Figure 30b. As is the case for the cold EqZ ensemble, a saturated water profile provides the starting point (solid line). Increasing the optical depth of the

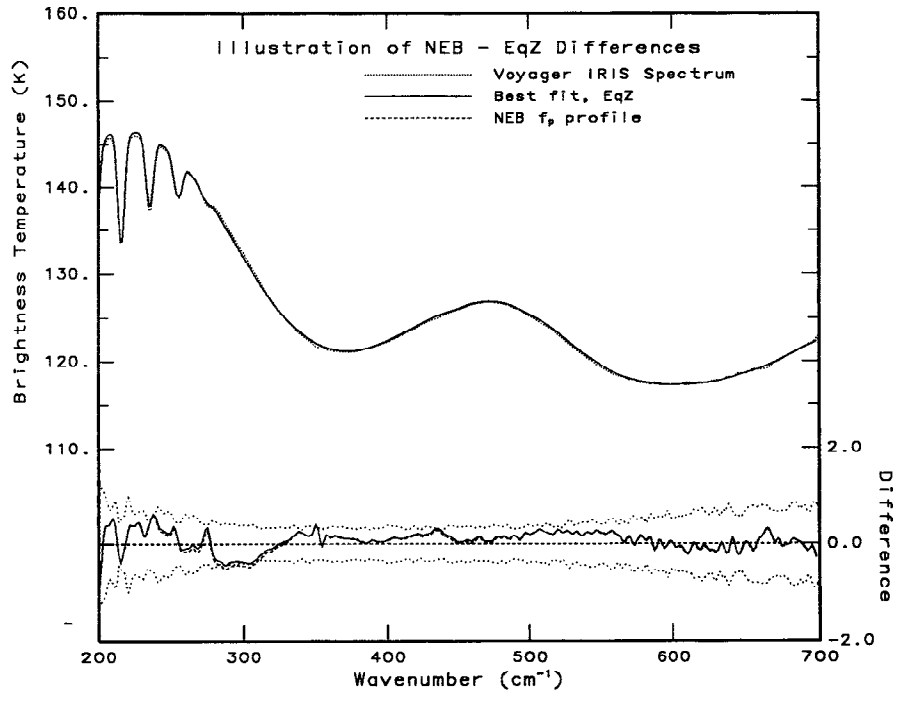


**Figure 29.** Comparison of the average IRIS cold EqZ spectrum (dotted line) with a synthetic spectrum (solid line) calculated using our best fit para hydrogen profile to the spectrum calculated using the NEB hot spot para hydrogen profile (dashed line).

$NH_4SH$ cloud to 3.1 and the optical depth of the $H_2O$ cloud to 15.0 (dashed line) improves the agreement between the synthetic and observed spectra. As was also the case in the cold EqZ, the vertical extent of the $NH_4SH$ cloud has to be increased to improve the fit to the slope of the continuum in the 1800–1950 cm$^{-1}$ region (dash-dot line). Since this pushes $NH_4SH$ cloud opacity to lower pressures, where it influences the far infrared, the 900–1200 cm$^{-1}$ region provides additional constraints on the optical depth of the $NH_4SH$ cloud.

Figure 31 shows the spectral sensitivity to the $NH_3$ vapor profile. If the vapor-to-gas scale height ratio is as small as 0.10 (dashed line), our best fit NEB hot spot value, there are some difficulties fitting selected frequencies in the 900–1000 cm$^{-1}$ region. Increasing the vapor-to-gas scale height ratio to 0.18 (dash-dot line), our best fit to the cold EqZ ensemble results in a poor fit to the depths of the $NH_3$ absorption features. Thus we find that $H_v/H_g$ has to be intermediate between these values, with 0.15 (solid line) providing a reasonable compromise between the depths of the absorption features and the fit to the continuum.

Similarly, these measurements provide some constraints on the vertical distribution of $PH_3$ above the 1-bar level. Figure 32 shows the spectral sensitivity to the $PH_3$ profile, values between 0.15 (dashed line) and 0.45 (dash-dot line) provide an acceptable fit to these NTrZ measurements, with 0.30 (solid line) representing our best fit.

The remaining model parameter is the hydrogen para fraction profile. In this case the IRIS NTrZ measurements do not provide tight constraints on the vertical distribution of para hydrogen. Nevertheless, as shown in Figure 33, the IRIS measurements are sufficient to constrain the location of the para hydrogen gradient to the upper troposphere. As shown, shifting the location of $P_L$ from 0.4 bar (solid line) to 0.7 bar (dashed line) results in an unacceptable fit to the IRIS measurements. The larger para fractions produce too much absorption. In contrast, if the para fraction retained its high-temperature equilibrium value of 0.25 to pressures as low as 0.2 bar, then the synthetic spectrum would contain too little absorption in the S(0) line region. Thus the transition between the high-temperature equilibrium value of 0.25 and the more equilibrated cloud-top value occurs in the upper troposphere, with our best fit profile specified by $P_L = 0.4 \pm 0.1$ bar, $P_U = 0.2 \pm 0.1$ bar, and $f_p = 0.35 \pm 0.03$ at pressures less than $P_U$. Our best fit parameters to the NTrZ ensemble are summarized in Table 4.

### 4.4. Summary

In the previous subsections, we presented the results of our analysis of the extreme spectral ensembles. These results are summarized in Table 4. Based on the characteristics of the IRIS measurements discussed in section 2 and the results of this analysis, we find that hot spot regions are unique to belts.

Consistent with the concept that hot spots correspond to regions of locally intense downwelling, we find that optical depths of all three clouds are reduced in these regions. In addition, we find that the $NH_3$ profile within and above the $NH_3$ cloud is more subsaturated in these regions than elsewhere. Similarly, we find that the relative humidity of water is reduced in the 2- to 4-bar region. In contrast, extreme zone ensembles have larger cloud optical depths, more $NH_3$ in the upper troposphere, and a saturated water profile. Moreover, consistent with the concept of upwelling motions in zones, we find that the vertical extent of the $NH_4SH$ and $H_2O$ clouds have to be increased in order to fit the slope of the IRIS measurements in the 1800–1950 cm$^{-1}$ region. The strength of the upwelling appears, based on the

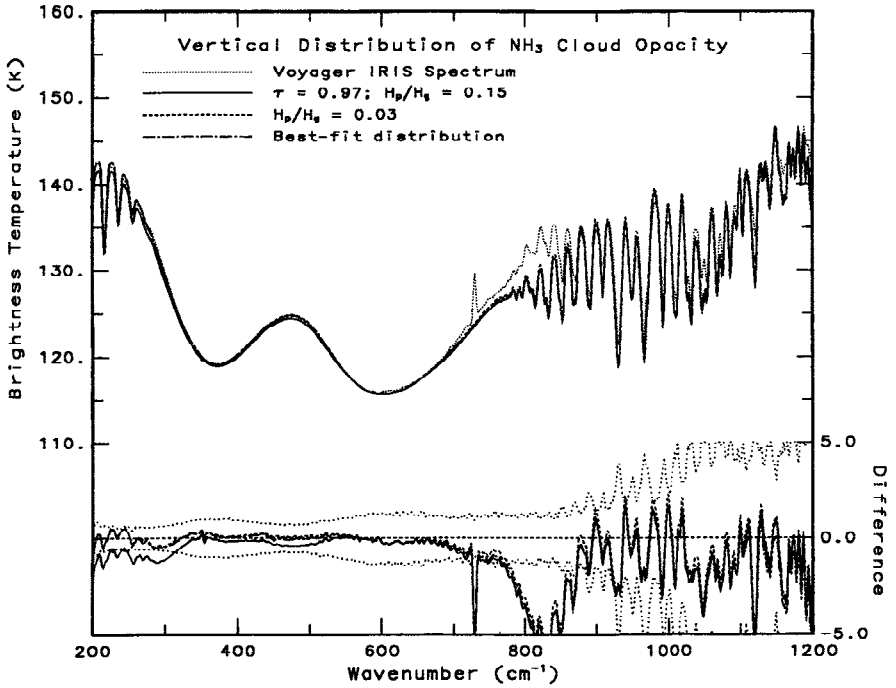


**Figure 30a.** NTrZ cloud structure. Comparison of the average IRIS cold NTrZ spectrum (dotted line) with synthetic spectra calculated with the optical depth of the $NH_3$ cloud increased to 0.97 and $H_p/H_g$ = 0.15 (solid line), with $H_p/H_g$ = 0.03 (dashed line), and with a slightly more complex optical depth distribution (dash-dot line) for the far-infrared.

larger abundance of $PH_3$ at pressures less than 1 bar and the larger $NH_3$ abundance within and above the $NH_3$ cloud, to be largest in the cold EqZ, where the cold ensemble undoubtedly contains measurements of the plume regions.

The para hydrogen profile is also consistent with these differences. In belts, the para hydrogen gradient is located between 0.2 and 0.5 bar, while in zones the lower inflection point is shifted to 0.4 bar. Since the $NH_3$ cloud base forms at

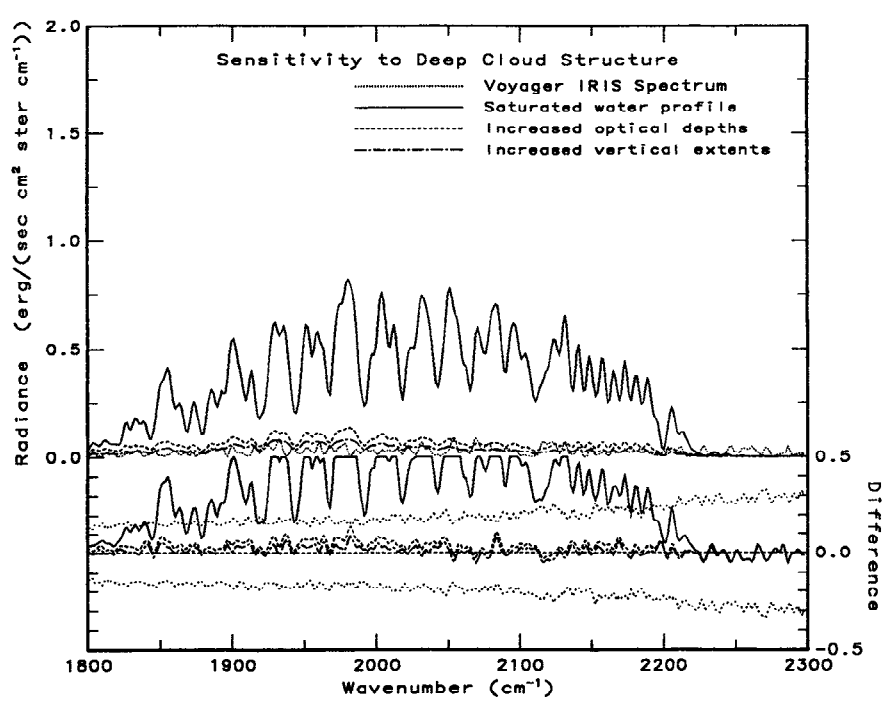


**Figure 30b.** Comparison of the average IRIS cold NTrZ spectrum (dotted line) with the NEB hot spot optical depths for the $NH_4SH$ and $H_2O$ clouds but with a saturated water profile (solid line), with the optical depths of the $NH_4SH$ and $H_2O$ clouds increased to 3.1 and 15.0, respectively (dashed line), and with the vertical extent of the $NH_4SH$ cloud increased ($H_p/H_g$ = 0.4) and the vertical extent of the $H_2O$ cloud increased ($H_p/H_g$ = 0.25) (dash-dot line).

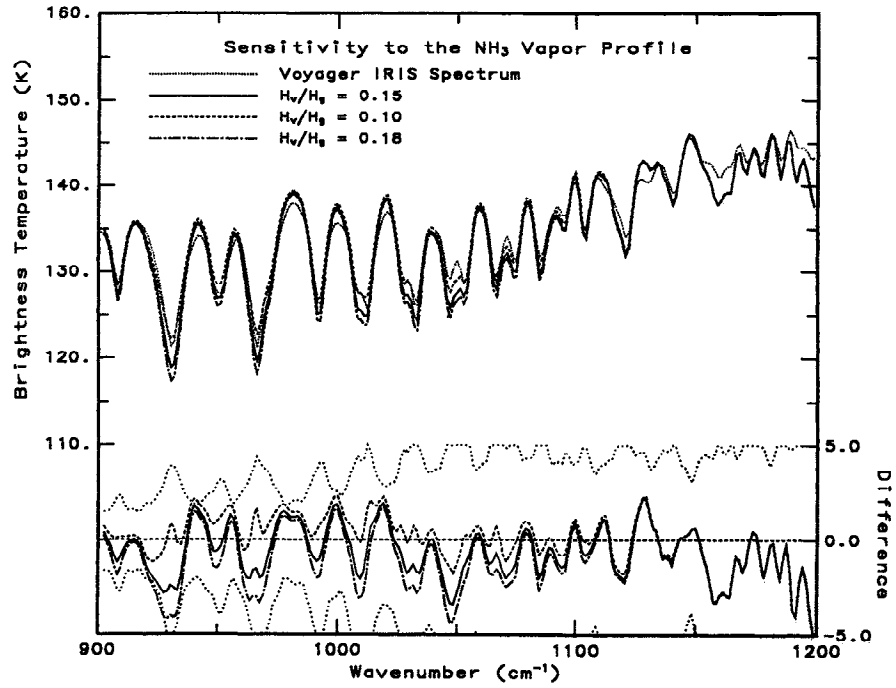


**Figure 31.** Sensitivity to the $NH_3$ profile in the NTrZ. The average IRIS cold NTrZ spectrum (dotted line) is compared with synthetic spectra calculated with an $NH_3$ vapor-to-gas scale height ratio of 0.15 (solid line; best fit), 0.10 (dashed line; NEB hot spot best fit value), and 0.18 (dash-dot line; cold EqZ best fit).

roughly the same pressure in both belts and zones, this shift suggests that upwelling motions (or stronger dynamical mixing) occur in zones and that dynamic transports are somewhat more rapid than ortho-para equilibration processes near the $NH_3$ cloud base in zones [*Carlson et al.*, 1992b]. The correlation of the para fraction near the $NH_3$ cloud top with the total $NH_3$ cloud optical depth suggests that the equilibration process predominates over dynamics there.

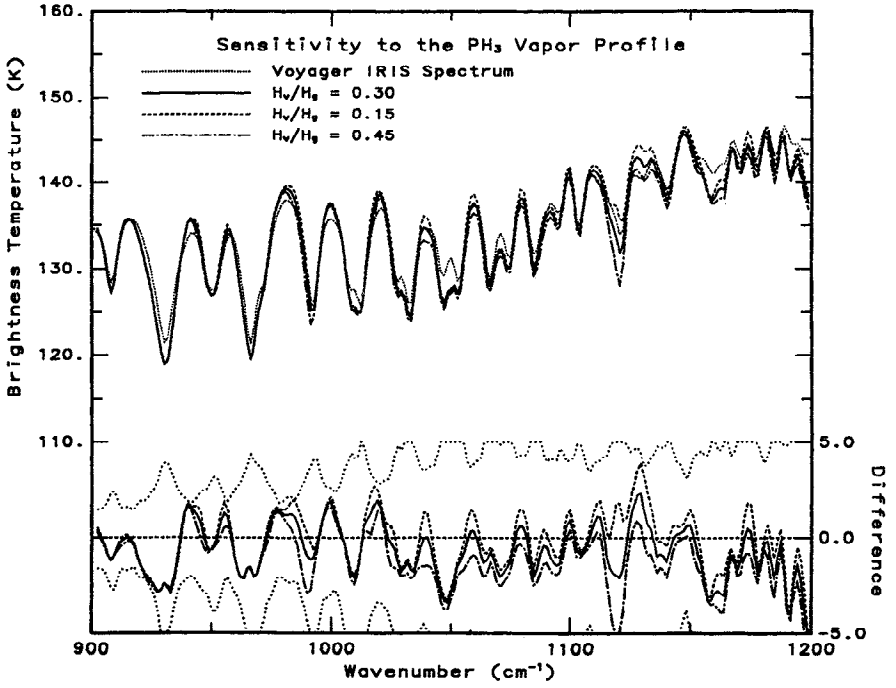


**Figure 32.** Sensitivity to the $PH_3$ profile in the NTrZ. The average IRIS cold NTrZ spectrum (dotted line) is compared with synthetic spectra calculated with a $PH_3$ distribution specified $H_v/H_g = 0.30$ (solid line), 0.15 (dashed line), and 0.45 (dash-dot line) at pressures less than 1 bar.

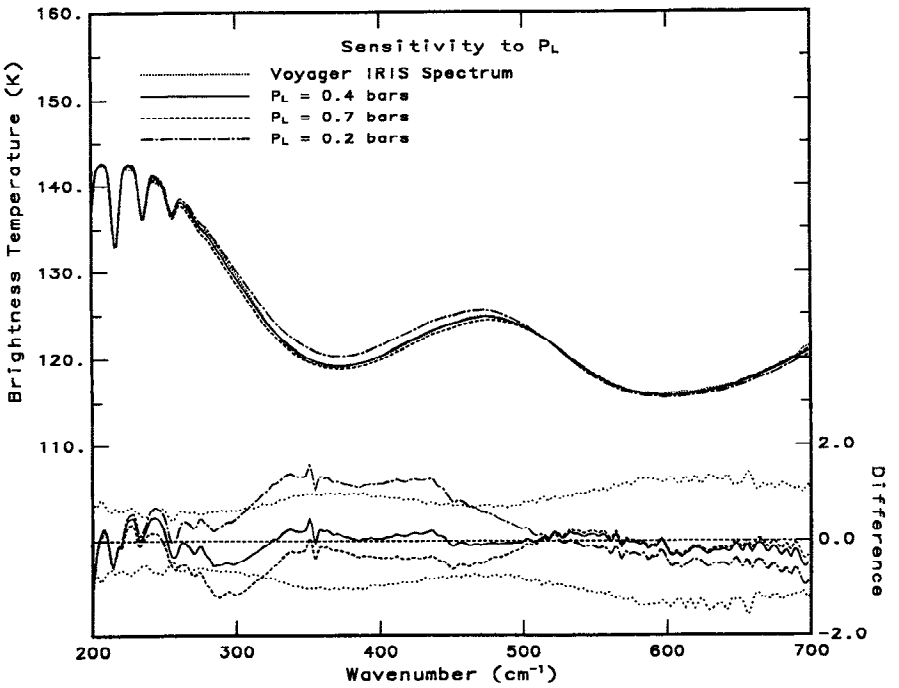


**Figure 33.** Sensitivity to the ortho-para profile in the NTrZ. The average IRIS cold NTrZ spectrum (dotted line) is compared with synthetic spectra calculated with $P_L$ = 0.4 bar (solid line; our best fit), 0.7 bar (dashed line), and 0.2 bar (dash-dot line). The difference between the synthetic and observed spectra is shown in the lower portion of the figure.

## 5. Implications

### 5.1. Coloration of Jupiter

*Young* [1985] examined photometrically corrected images of Jupiter and commented on the overall bland appearance of the planet. On the whole, the planet appears pale yellowish gray with contrasts no more than about 10%. It is quite likely therefore that the differences in the coloration of belts and zones can be explained by differences in cloud opacity that affect the depth of penetration of visible light. Above the tropospheric cloud layers that we have been focusing on is a stratospheric aerosol or haze layer [*Smith*, 1980; *West*, 1988]. The optical depth of the haze layer has been estimated to be of the order of hundredths at visible wavelengths [*West*, 1988; *Smith and Tomasko*, 1984]; thus our omission of this small amount of opacity associated with the stratospheric aerosol layer will not appreciably alter the location of unit optical depth at visible wavelengths in the following discussion. The total range of $NH_3$ cloud opacity is only from 0.27 to 0.98, equivalent to the variations of "thin" cirrus on Earth and is not large enough to explain the observed contrast variations.

In the zones the optical depth of the $NH_3$ cloud varies from 0.42 in our hot EqZ ensemble to 0.98 in the cold NTrZ ensemble and the optical depth of the $NH_4SH$ cloud varies from 0.5 to 5.3. Thus unit extinction optical depth (at the reference wavelength of 0.5 $\mu$m) varies from well within to just above the $NH_4SH$ cloud in zones. Laboratory experiments have shown that yellow polysulfides form when $NH_4SH$ is irradiated by UV light [*Sill*, 1973; *Huntress and Thorne*, 1982; *Huntress and Anicich*, 1984]. The vertical profile of $PH_3$ suggests its depletion by photochemistry down to the 1-bar level. Since the $NH_4SH$ cloud is mixed with the $NH_3$ cloud at pressures <0.5 bar in some portions of the zones, some UV radiation may penetrate to the $NH_4SH$ cloud. Thus the pale yellow coloration of zones may be due to such polysulfides produced on the $NH_4SH$ particles, and subtle variations in color would be associated with changes in the $NH_3$ cloud opacity.

In belts, $NH_3$ and $NH_4SH$ clouds are much thinner, optical depths ranging from 0.27 and 0.02 in hot spots to 0.8 and 4.0 in the coldest NEB ensemble, respectively. Thus the unit extinction optical depth varies from within the $NH_4SH$ cloud layer to within the $H_2O$ cloud, and where sunlight reaches deeper levels, the photolysis products of $H_2S$ might provide additional chromophores and/or chemical reactions in the water cloud that might affect the coloration. Variations in the optical depths of the $NH_3$ and $NH_4SH$ clouds, at least, are required to explain the different mottled appearance of the NEB at the time of the Voyager flybys. There is no indication that the abundance of $H_2S$ is larger in belts than in zones, since in both regions the nondetection of $H_2S$ is consistent with the upper limit determined by *Larson et al.* [1984] and with the formation of an $H_2S$-containing condensate in the 2-bar region of the atmosphere. The greater transparency of the $NH_3$ and $NH_4SH$ clouds in some belt regions can account for the color contrast by allowing sunlight to penetrate to the water cloud level.

Aqueous chemical reactions produce significant amounts of sulfur ions [*Carlson et al.*, 1987], so that the even darker coloration in regions where the overlying cloud opacity is low, e.g., hot spots, could be caused by sulfur ions in solution [*West et al.*, 1985] which have the requisite strong spectral gradient near 0.6 $\mu$m [*Chivers*, 1977; *Salahub et al.*, 1978].

These results support the model proposed by *Owen and Terrile* [1981] to explain the Voyager imaging observations.

The presence of chromophores mixed throughout the upper tropospheric clouds is also consistent with conclusions regarding the vertical distribution of chromophores based on the analysis of the Pioneer polarimetry and photometry [*Smith and Tomasko*, 1984]. However, our results contradict the fundamental assumption of the Pioneer cloud models that the $NH_3$ cloud forms a semi-infinite lower boundary condition for visible radiation. In all cases, we find that the optical depth of the $NH_3$ cloud is less than unity. In addition, since we find that the optical depth of the $NH_4SH$ cloud varies from 0.02 to 5.3, this cloud should also be explicitly modeled in the analysis of reflected solar radiation. As suggested by *Marten et al.* [1981] and *Bézard et al.* [1983], it is the spatial variations in the optical depth of the $NH_4SH$ cloud that account for most of the observed variations in the 5-$\mu$m brightness temperatures. Our results suggest that it is only the water cloud that could be treated as a semi-infinite lower boundary in the analysis of reflected solar radiation. Thus it would be interesting to see a reanalysis of reflected solar measurements of Jupiter that examines the influence of the semi-infinite lower boundary assumptions on the results.

The low optical depths of the $NH_3$ cloud also require that the visible albedo features in Pioneer and Voyager images are produced primarily by variations in the deeper clouds. Although unit extinction optical depth occurs in the vicinity of the $NH_4SH$ cloud, the visible albedo continues to vary strongly as total optical depth is increased from 1 to over 50. Thus a large change in the optical depth of the water cloud, from 10 to 15, say, would be visible as a significant albedo change even in the NTrZ.

This conclusion has implications for interpretation of cloud-tracked wind analyses which normally assume that the cloud features being tracked are located near the 0.3-bar level [cf. *Gierasch et al.*, 1986]. These analyses also assume that the "cloud" altitude is latitudinally invariant, yet the most important cloud variations may be at much higher pressure in belts than in zones, casting some doubt on interpretations of horizontal wind shears. The effective location of the wind speeds inferred from the motions of these features is, at best, ambiguous and probably at higher pressures than usually assumed, implying that estimates of the vertical wind shear are only upper limits.

### 5.2. Atmospheric Circulation

The variations of the basic features of the gas distributions and cloud properties (optical depths and vertical extents) found in our analysis are all consistent with the interpretation that zones are general regions of upwelling and belts are general regions of downwelling in the mean circulation. The correlated behavior of all three clouds suggests that this mean circulation extends from $NH_3$ cloud levels down to at least the water cloud level. That it is the mean circulation that is responsible for the belt-zone structures is supported by the facts that the "hot" extreme spectral ensemble is unique to belts and the "cold" extreme spectral ensemble is unique to zones, but that intermediate spectral ensembles are common to both regions.

The vertical correlation between the location of the $NH_3$ cloud layer and the para hydrogen gradient supports the conclusion of *Massie and Hunten* [1982] that paramagnetic conversion on $NH_3$ cloud particles is the dominant equilibration process for hydrogen in the upper troposphere. However, the differences in horizontal variations at cloud top and cloud base between and within the zones and belts suggest that dynamic mixing predominates over ortho-para conversion near cloud base but not at cloud top [*Carlson et al.*, 1992b]. The Massie and Hunten model for ortho-para equilibration places constraints on the magnitude of the dynamical mixing rates, which they represent by an eddy diffusion coefficient. For complete equilibration, the eddy diffusion coefficient must be $<10^6$ cm$^2$/s. The horizontal variations in para fraction profiles imply a belt-zone variation in the location and magnitude of the rapid mixing regime. If we consider the "convective" regime in the Jovian atmosphere to correspond to an eddy diffusion coefficient of roughly $10^8$ cm$^2$/s [*Prinn and Barshay*, 1977], then our results suggest a belt-zone variation in the location of the radiative-convective boundary from a pressure at or greater than 0.55 bar to about 0.4 bar.

The larger horizontal variations and vertical extent of the $NH_3$ cloud (indicated by the increased range of observed 45- and 5-$\mu$m brightness temperatures) in the EqZ observations compared with the NTrZ suggest a stronger influence of smaller-scale motions on the cloud, possibly associated with penetrative moist convection overshooting into the $NH_3$ cloud layer [*Del Genio and McGrattan*, 1990]. Based on our analysis of the IRIS measurements, convection extends to at least the 0.4-bar level, based on the location of the para hydrogen gradient. The results of Del Genio and McGrattan suggest that convective overshooting to the 0.3-bar level is possible in plumes driven by moist convection. (The observed plume features do not need to extend above the $NH_3$ cloud, since such a cloud would easily be visible through the $NH_3$ cloud in the EqZ, which has an optical depth $<1$.) The EqZ para hydrogen profile is similar to that in the NTrZ, although the degree of equilibration is less, which when combined with the increased $NH_3$ relative humidity and the larger abundances of $PH_3$ at pressures less than 1 bar, all suggest enhanced upwelling motions in the cold EqZ regions. Moreover, the presence of regions within the EqZ with average 5-$\mu$m brightness temperatures in excess of 230 K is also suggestive of the presence of stronger wave activity. These regions are also associated with reduced relative humidity that may indicate dynamic drying and localized downwelling motions, which are expected to be associated with the stronger penetrative convection.

Wave motions are also apparent in the variations in belts. A comparison between the extreme spectral ensembles within the NEB suggests that hot spots correspond to regions in which a wave downdraft reinforces the mean downwelling motions. In contrast, the colder extremes correspond to regions in which a wave updraft opposes the mean downwelling motions, resulting in a weak updraft. That the strength of the updraft is weaker than the mean upwelling present in zones is indicated by the smaller $NH_3$ cloud optical depth and vertical extent.

Thus we conclude that the observed spatial variations of 45- and 5-$\mu$m brightness temperatures and their correlations can be explained by a plausible superposition of a mean circulation responsible for the planetary-scale belt-zone structure and wave motions responsible for the horizontal variations within the individual belts and zones. That the extreme spectral ensembles are unique to either belts or zones, where wave motions reinforce the mean circulation, and intermediate spectral ensembles are similar in both belts and zones, where wave motions oppose the mean circulation, requires that the strength

of these two kinds of motion be comparable. The presence of wave motions can also account for the temporal variations in the Jovian cloud structure without any variation in the mean zonal jets, as observed. Relative humidity variations alone, in the absence of any cloud opacity variations, such as the change from our dry NEB hot spot humidity profile to a saturated profile, would only produce a 5°C decrease in the average 5-$\mu$m brightness temperature. Thus the larger magnitude of the variations reported by *Terrile and Westphal* [1977], in which 5-$\mu$m features have been observed to form or disappear in the course of a few rotations, require both humidity and cloud opacity variations. These opacity variations have to occur in the deeper clouds, since the $NH_3$ cloud has only a small effect on 5-$\mu$m radiation.

**Acknowledgments.** We thank R. Hanel and the Voyager IRIS team for designing such a beautiful instrument and obtaining one of the finest planetary data sets. We thank A. D. Del Genio and L. D. Travis for many helpful discussions and A. Wolf and A. Wasilewski for help with the figures. We would like to acknowledge the support of the Planetary Atmospheres Discipline, NASA Office of Space Science and Applications.

## References

Bézard, B., J. P. Baluteau, and A. Marten, Study of the deep cloud structure of the equatorial region of Jupiter from Voyager infrared and visible data, *Icarus*, *54*, 434–455, 1983.

Bjoraker, G. L., H. P. Larson, and V. G. Kunde, The abundance and distribution of water vapor in Jupiter's atmosphere, *Astrophys. J.*, *311*, 1058–1072, 1986.

Carlson, B. E., M. J. Prather, W. B. Rossow, Cloud chemistry on Jupiter, *Astrophys. J.*, *322*, 559–572, 1987.

Carlson, B. E., W. B. Rossow, and G. S. Orton, Cloud microphysics of the giant planets, *J. Atmos. Sci.*, *45*, 2066–2081, 1988.

Carlson, B. E., A. A. Lacis, and W. B. Rossow, The abundance and distribution of water vapor in the Jovian troposphere as inferred from Voyager IRIS observations, *Astrophys. J.*, *388*, 648–668, 1992a.

Carlson, B. E., A. A. Lacis, and W. B. Rossow, Ortho-para hydrogen equilibration on Jupiter, *Astrophys. J.*, *393*, 357–372, 1992b.

Carlson, B. E., A. A. Lacis, and W. B. Rossow, Tropospheric gas composition and cloud structure of the Jovian north equatorial belt, *J. Geophys. Res.*, *98*, 5251–5290, 1993.

Chivers, T., Polychalcogenide anions, in *Homoatomic Rings, Chains and Macromolecules of Main-Group Elements: Proceedings of the IX Hudson Symposium*, edited by A. L. Rheingold, pp. 499–537, Elsevier, New York, 1977.

Conrath, B. J., R. A. Hanel, V. G. Kunde, and C. P. Prabhabara, The infrared interferometer experiment on Nimbus 3, *J. Geophys. Res.*, *75*, 5831–5857, 1970.

Del Genio, A. D., and K. B. McGrattan, Moist convection and the vertical structure and water abundance of Jupiter's atmosphere, *Icarus*, *84*, 29–53, 1990.

Fountain, J. W., D. L. Coffeen, L. R. Doose, T. Gehrels, W. Swindell, and M. G. Tomasko, Jupiter's clouds: Equatorial plumes and other cloud forms in the Pioneer 10 images, *Science*, *184*, 1279, 1974.

Gautier, D., B. Conrath, M. Flasar, R. Hanel, V. Kunde, A. Chedin, and N. Scott, The helium abundance of Jupiter from Voyager, *J. Geophys. Res.*, *86*, 8713–8720, 1981.

Gehrels, T., The results of the imaging photopolarimeter on Pioneers 10 and 11, in *Jupiter*, edited by T. Gehrels, pp. 531–563, University of Arizona Press, Tucson, 1976.

Gierasch, P., B. J. Conrath, and J. A. Magalhaes, Zonal mean properties of Jupiter's upper troposphere from Voyager infrared observations, *Icarus*, *67*, 456–483, 1986.

Hanel, R., et al., Infrared observations of the Jovian system from Voyager 1, *Science*, *204*, 972–976, 1979.

Hansen, J. E., and L. D. Travis, Light scattering in planetary atmospheres, *Space Sci. Rev.*, *16*, 527–610, 1974.

Hess, S. L., and H. A. Panofsky, The atmospheres of the other planets, in *Compendium of Meteorology*, pp. 391–400, American Meteorological Society, Boston, Mass., 1951.

Huntress, W. T., Jr., and V. G. Anicich, Colored sulfur species in the atmosphere of Jupiter, *Bull. Am. Astron. Soc.*, *16*, 648, 1984.

Huntress, W. T., Jr., and L. Thorne, Colored sulfur ions in the atmosphere of Jupiter, *Bull. Am. Astron. Soc.*, *14*, 723, 1982.

Kunde, V. G., and W. C. Maguire, Direct integration transmittance model, *J. Quant. Spectrosc. Radiat. Transfer*, *14*, 803–817, 1974.

Kunde, V., R. Hanel, W. Maguire, D. Gautier, J. P. Baluteau, A. Marten, A. Chedin, N. Husson, and N. Scott, The tropospheric gas composition of Jupiter's north equatorial belt ($NH_3$, $PH_3$, $CH_3D$, $GeH_4$, $H_2O$) and the Jovian D/H isotopic ratio, *Astrophys. J.*, *263*, 443–467, 1982.

Larson, H. P., D. S. Davis, R. Hofman, and G. L. Bjoraker, The Jovian atmospheric window at 2.7 $\mu$m: A search for $H_2S$, *Icarus*, *60*, 621–639, 1984.

Lutz, B. L., and C. A. Gullixson, Jupiter, *IAU Circ. 4861*, Int. Astron. Union, Dordrecht, Netherlands, 1989.

Marten, A., D. Rouan, J. P. Baluteau, D. Gautier, B. J. Conrath, R. A. Hanel, V. Kunde, R. Samuelson, A. Chedin, and N. Scott, Study of the ammonia ice cloud layer in the equatorial region of Jupiter from the infrared interferometric experiment on Voyager, *Icarus*, *46*, 233–248, 1981.

Massie, S. T., and D. M. Hunten, Conversion of para and ortho hydrogen in the Jovian planets, *Icarus*, *49*, 213–226, 1982.

Owen, T., and R. J. Terrile, Colors on Jupiter, *J. Geophys. Res.*, *86*, 8787–8814, 1981.

Prinn, R. G., and S. S. Barshay, Carbon monoxide on Jupiter and implications for atmospheric convection, *Science*, *198*, 1031–1034, 1977.

Salahub, D. R., A. E. Fotti, and V. H. Smith Jr., Molecular orbital study of the structural changes on oxidation and reduction of $S_3$, $S_4$, $S_6$, and $S_8$, *J. Am. Chem. Soc.*, *100*, 7847–7859, 1978.

Sill, G. T., Reflection spectra of solids of planetary interest, *Commun. Lunar Planet. Lab.*, *10*, 1–7, 1973.

Smith, B. A., et al., The Jupiter system through the eyes of Voyager 1, *Science*, *204*, 951–971, 1979.

Smith, D. W., Galilean satellite eclipse studies, II, Jovian stratospheric and tropospheric aerosol content, *Icarus*, *44*, 116–133, 1980.

Smith, P. H., and M. G. Tomasko, Photometry and polarimetry of Jupiter at large phase angles, II, Polarimetry of the south tropical zone, south equatorial belt, and the polar regions from the Pioneer 10 and 11 mission, *Icarus*, *58*, 35–73, 1984.

Stone, P. H., The meteorology of the Jovian atmosphere, in *Jupiter*, edited by T. Gehrels, pp. 586–618, University of Arizona Press, Tucson, 1976.

Terrile, R. J., and J. A. Westphal, The vertical cloud structure of Jupiter from 5 $\mu$m measurements, *Icarus*, *30*, 274–281, 1977.

Weidenschilling, S. J., and J. S. Lewis, Atmospheric and cloud structures of the Jovian planets, *Icarus*, *20*, 465–476, 1973.

West, R. A., Voyager 2 imaging eclipse observations of the Jovian high altitude haze, *Icarus*, *75*, 381–398, 1988.

West, R. A., P. N. Kupferman, and H. Hart, Voyager 1 imaging and IRIS observations of Jovian methane absorption and thermal emission: Implications for cloud structure, *Icarus*, *61*, 311–342, 1985.

West, R. A., D. F. Strobel, and M. G. Tomasko, Clouds, aerosols and photochemistry in the Jovian atmosphere, *Icarus*, *65*, 161–217, 1986.

Williams, G. P., Jovian and comparative atmospheric modeling, in Issues in Atmospheric and Oceanic Modeling, Part A: Climate Dynamics, edited by S. Manabe, *Adv. Geophys.*, *28A*, 381–432, 1985.

Young, A. T., What color is the solar system?, *Sky Telescope*, May, 399–402, 1985.

B. E. Carlson, A. A. Lacis, and W. B. Rossow, NASA Goddard Institute for Space Studies, 2880 Broadway, New York, NY 10025.

(Received March 18, 1992; revised March 21, 1994; accepted May 6, 1994.)